A homotopy for the reliable estimation of model parameters in chromatography processes

Dominik H. Cebulla[a,*], Christian Kirches[a], Nico Kümmerer[b], Andreas Potschka[c]

[a] *Institute for Mathematical Optimization, Technische Universität Braunschweig, 38106 Braunschweig, Germany*
[b] *Recombinant Research & Development, Octapharma Biopharmaceuticals GmbH, Im Neuenheimer Feld 590, 69120 Heidelberg, Germany*
[c] *Institute of Mathematics, Clausthal University of Technology, 38678 Clausthal–Zellerfeld, Germany*

Abstract

Mathematical modeling, simulation, and optimization can significantly support the development and characterization of chromatography steps in the biopharmaceutical industry. Particularly mechanistic models become preferably used, as these models, once carefully calibrated, can be employed for a reliable optimization. However, model calibration is a difficult task in this context due to high correlations between parameters, highly nonlinear models, and limited prior knowledge of certain parameters, among others.

In this work we propose a homotopy-based globalization strategy that can be used in combination with iterative algorithms for the solution of mathematical optimization problems, particularly parameter estimation problems. With our approach, convergence can be achieved even when initial guesses are far away from a solution. Moreover, we describe and discuss the calibration procedure for a real-world ion exchange chromatography process, here considering a complete chromatography system. This description may serve as a general blueprint for the estimation of model parameters in chromatography processes.

Keywords: Model calibration, Globalization, Homotopy methods, Chromatography
2010 MSC: 35Q93, 65H20, 92C40

1. Introduction

The biopharmaceutical industry is fast growing and highly competitive. More drug candidates must be developed in a shorter period of time while also maintaining high quality standards, e.g., in terms of purity of the desired product. Hence, the purification process of biopharmaceuticals, also called downstream process, must adapt quickly to new molecules in a short amount of time and with limited sample volumes.

Column chromatography is predominantly used in the downstream processing of biopharmaceuticals. This technique is versatile and still subject to major developments, compare Unger et al. (2010) and Rathore et al. (2018). However, to effectively and efficiently make use of chromatography

*Corresponding author
Email addresses: d.cebulla@tu-bs.de [ORCID 0000-0002-3025-8673] (Dominik H. Cebulla), c.kirches@tu-bs.de [ORCID 0000-0002-3441-8822] (Christian Kirches), nico.kummerer@octapharma.com (Nico Kümmerer), andreas.potschka@tu-clausthal.de [ORCID 0000-0002-6027-616X] (Andreas Potschka)

steps, a substantial process understanding is required, which is also promoted by regulatory agencies such as the U.S. Food and Drug Administration. In their guidelines for process development, compare U.S. Food and Drug Administration (2004), it is also stated that the ability to predict the process behavior shows a deeper understanding of the underlying process and may therefore lead to more freedom in changing the originally approved process conditions.

Since chromatography steps make up to 70% of the total costs in the downstream processing (Osberghaus et al., 2012a), there is a large interest in the optimization of such processes. Both economic and ecological benefits can be expected, such as a shorter process duration, improved product quality, and an economic use of buffer components. In the last few decades, techniques from mathematical optimization have been employed to successfully optimize chromatographic separation processes, compare, e.g., Karlsson et al. (2004), Nfor et al. (2011), Holmqvist et al. (2015), Pirrung et al. (2017), Bock et al. (2021), and Cebulla et al. (2023). Albeit typically being more complex than, e.g., empirical models, the use of mechanistic models becomes increasingly preferred, as such models typically exhibit a good predictability (Osberghaus et al., 2012b). Indeed, quite a few mechanistic mathematical models have been proposed to describe different types of chromatographic processes, such as size exclusion chromatography, ion exchange chromatography, hydrophobic interaction chromatography, multimodal chromatography, and affinity chromatography, compare the books by Guiochon et al. (2006) and Schmidt-Traub et al. (2012), as well as, e.g., Brooks and Cramer (1992), Nfor et al. (2010), Deitcher et al. (2010), Sandoval et al. (2012), Nilsson and Andersson (2017), Leweke and von Lieres (2018, table 1), and Cebulla et al. (2019).

However, the calibration of mechanistic models is a challenging task, due to highly nonlinear models, high correlations between certain model parameters, and a lack of sufficient data, compare Rischawy et al. (2019). In this work, we propose a new methodology that can be used in combination with an iterative optimization algorithm for a reliable estimation of model parameters for chromatographic processes.

1.1. Related work

Various methods have been proposed for the estimation of model parameters of a mechanistic model, e.g., use of correlations, as well as performance and evaluation of tracer, frontal, and bind-and-elute experiments, compare Schmidt-Traub et al. (2012, section 6.5) and Gu (2015, chapter 4), as well as the references cited therein.

Furthermore, parameters related to mass transfer phenomena, such as dispersion, diffusion, and (film) mass transfer coefficients, can be either estimated by evaluation of breakthrough curves (Persson et al., 2006) or by a moment analysis of performed tracer experiments in combination with correlations, compare Schmidt-Traub et al. (2012, sections 6.5.3.1, 6.5.6.2, and 6.5.8). Estimation of model parameters for column external equipment, such as additional mixers and tubing, can be performed in a similar way.

However, it is typically the adsorption-related model parameters that affect the elution profiles in chromatograms the most. It is hence crucial to take particular care when estimating these model parameters. Again, several methods have been proposed in the past. For example, Brooks and Cramer (1992) describe a strategy to determine equilibrium parameters for their proposed steric mass action (SMA) isotherm model to describe ion exchange chromatography (IEX) processes. One further parameter occurring in this model, namely the total ionic capacity, can be either retrieved from manufacturer data or from titration experiments, compare Tugcu et al. (2002). Further approaches, e.g., for the determination of saturation capacities and Henry coefficients, are summarized in Schmidt-Traub et al. (2012, section 6.5.7). Also, manually fitting certain model parameters to

given measurement data has been reported to yield promising results, compare Karlsson et al. (2004).

A different strategy for the estimation of model parameters that is also independent of the actually employed mathematical model is the use of an inverse method. Here, a mathematical optimization problem has to be solved where the objective is to minimize an appropriately defined deviation between measurement data and model prediction; the model parameters are the degrees of freedom. The probably most famous problem class are least squares problems, where the squared difference between measurements and predictions are minimized.

Inverse methods are often used to estimate adsorption-related parameters, compare Nfor et al. (2010), Schmidt-Traub et al. (2012, section 6.5.7.11), Leweke and von Lieres (2018), and Rischawy et al. (2019). Osberghaus et al. (2012a) have shown for the SMA isotherm model that both approaches, namely either following the instructions by Brooks and Cramer (1992) or using an inverse method, yield comparable results with respect to the predictability of the calibrated model. Yet, the obtained parameter values were not the same. Although the authors seem to favor the inverse method for the ability of fast process development, this approach also has its limitations. For example, it is generally agreed that one should not try to estimate all model parameters simultaneously with an inverse method, as high correlations between certain parameters may lead to meaningless results, compare Leweke and von Lieres (2018) and Rischawy et al. (2019). Indeed, some authors state that no more than three parameters should be estimated simultaneously with this approach, compare Schmidt-Traub et al. (2012, section 6.5.3.2). Therefore, as many parameters as possible should still be determined separately, e.g., with the methods summarized at the beginning of this section.

To numerically solve the (least squares) parameter estimation problems, the current state of the art is using heuristic approaches, such as sampling, genetic algorithms or simulated annealing, in order to obtain good starting points for a successive refined search by a derivative-based optimization algorithm, such as the Levenberg-Marquardt method or an interior point method (IPM), compare Wang et al. (2016), Leweke and von Lieres (2018), and Rischawy et al. (2019).

1.2. Contribution

Based on the previous discussion, we can see that application of an inverse method is an important ingredient for the estimation of model parameters. However, the performance of these methods typically relies on a "good" initial guess provided by the user. For some model parameters good initial guesses can be obtained by using correlations, but for other parameters, specifically adsorption-related ones, not even the order of magnitude may be known. As stated in the previous section, an initial guess is often obtained by a heuristic approach, typically combined with the claim that this is done to avoid local minima. However, we must emphasize that using these heuristics does not guarantee to converge to a global minimum (yet, a better local optimum may be found). Even if a better local minimum in terms of the objective function value is obtained, the found minimizer is useless if it is not stable under perturbations of the measurements, compare Bock et al. (2007, section 3.5) and Bock et al. (2020, section 2). Lastly, in order to employ these heuristic approaches, the search space has to be limited beforehand, which might cut off desirable local minima.

In this work we propose a novel homotopy-based globalization approach for iterative methods, whose aim is to ensure convergence to a local solution even if the initial parameter guess is far away from a solution. Although we limited the previous discussion to mechanistic models, the proposed

methodology can in principle be also used when employing other types of models, such as empirical models.

To show and investigate properties of the proposed homotopy approach, we consider a real-world IEX process, for which we perform model calibration. We fully describe a procedure to estimate all occurring model parameters, which may serve as a general template for model calibration of chromatographic processes. Moreover, the homotopy approach is analyzed in terms of the parameter values along the homotopy path, as well as in terms of required number of iterations of a generalized Gauss–Newton method for solving (constrained) least squares problems.

1.3. Outline

The remainder of this article is organized as follows: In section 2 we introduce our novel homotopy-based globalization approach in a rather general framework, i.e., by not making assumptions on the type of mathematical model being used, as well as independent on the actual numerical method to solve parameter estimation problems. The estimation of model parameters for a real-world IEX process by using the novel homotopy approach is presented in section 3. We conclude with a discussion of the presented results in section 4.

2. Reliable parameter estimation in chromatographic applications using a homotopy-based globalization approach

The goal of this section is to introduce a novel homotopy-based globalization approach based on exponentially modified Gaussian (EMG) functions and tailored to chromatographic applications for the reliable estimation of unknown model parameters. To this end, we first describe the general setting and the problems that may occur in this context, followed by a presentation of the novel homotopy strategy to overcome these problems. Lastly, we discuss possible extensions to the proposed methodology and provide theoretical considerations regarding its local convergence behavior.

2.1. Setting and resulting difficulties

We first describe our setting for the estimation of model parameters for chromatographic applications.

Assumption 2.1. Let $\mathcal{T} = [t_0, t_f] \subseteq \mathbb{R}$ be the time horizon of interest and $\mathcal{P} \subseteq \mathbb{R}^{n_p}$ the space of admissible parameters. Our setting for parameter estimation is based on the following assumptions:

1. There are scalar-valued measurements $\eta_i = \eta(t_i) \in \mathbb{R}$ for selected time points $t_i \in \mathcal{T}$. We allow $t_i = t_j$ for $i \neq j$, hence there can be multiple measurements at a single point in time. In chromatographic applications measurement data is typically given in form of chromatograms, e.g., data from ultraviolet (UV) spectroscopy. We first limit our discussion to a single-component experiment where a single peak can be observed, compare figure 1.
2. There is a model response / prediction function $h\colon \mathcal{T} \times \mathcal{P} \to \mathbb{R}$ such that (ideally) we have $h(t_i, p) \approx \eta_i$ for a suitable choice of p and for all i. Evaluation of the model response function may involve the solution of a partial differential equation (PDE) model when using so-called rate models, but also empirical models can be used.
3. To estimate model parameters based on given measurements, certain instances of nonlinear programs (NLPs) must be solved, such as (weighted) least-squares or least absolute deviation problems. We assume that an *iterative* algorithm is used to solve such parameter estimation problems. This implies that we require an initial parameter value $p^{(0)} \in \mathcal{P}$ to start the solution procedure.

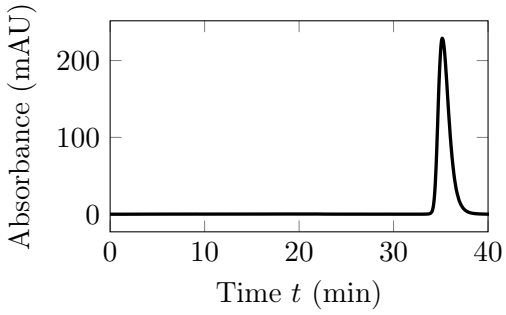

Figure 1: Exemplary data of a real-world chromatography experiment. Here, a single substance is investigated and the data shows a single peak.

We note that our setting is fairly general and by no means uncommon. However, the limitation to a single-component experiment with a single observable peak can be too restrictive in certain cases; specifically, if it is not feasible to perform single-component experiments. We therefore discuss later in section 2.3 possible extensions to the homotopy approach presented in section 2.2, including the multi-component case.

With the setting described in assumption 2.1, we identify the following potential difficulties, which were also briefly mentioned in section 1:

1. Some of the model parameters p may be completely unknown and vary over several orders of magnitude. The initially chosen parameter guess $p^{(0)}$ may therefore be far away from a solution and the employed NLP solver may require a large number of iterations until the respective termination criteria are fulfilled.
2. Some of the model parameters may be highly correlated or can only be determined under experimental conditions that are not always possible to conduct, such as experiments with high sample concentrations.
3. Available measurements are typically conductivity, pH, and UV absorbance of the fluid leaving the column. On the one hand, this implies that we cannot measure the concentration profiles of separate components, but, in the simplest case, only a weighted sum thereof, compare (10) in section 3.1. On the other hand, we also cannot measure the state *within* the chromatography column. Hence we obtain comparably little information from measurement data.
4. Depending on the employed mathematical models, bounds must be imposed on the parameters (and possibly further variables, such as concentrations) in order to guarantee non-negativity. Both (too) negative concentrations and parameters can lead to a breakdown of the employed solution method, as the underlying model response function h may not be evaluable anymore. On the other hand, imposing bound constraints may lead to very small steps taken by the employed NLP solver. An active set strategy, as previously proposed (Cebulla et al., 2019), may improve on this situation, but not on the other difficulties.

A combination of the above mentioned difficulties may lead to a breakdown of the employed solution strategy, i.e., the solver does not, or only very slowly, converge. To overcome this undesired behavior we propose a novel homotopy-based globalization approach whose description is the subject of the next section.

Algorithm 1: Generic homotopy approach for parameter estimation problems.

Input: Initial parameter estimate $p^{(0)}$, sequence of measurements $\{\eta^{(1)}, \dots, \eta^{(N)}\}$.
Output: Parameter estimate $p^{(N)}$ for the measurements $\eta^{(N)}$.

```
for k = 1 to N do
    Obtain parameter estimate p^(k) based on measurements η^(k) by applying a suitable
     inverse method / NLP solver. Use p^(k−1) (or a suitable predictor) as initial guess.
end
```

2.2. Homotopy-based globalization approach using exponentially modified Gaussian functions

To summarize the difficulties mentioned in the previous section, particularly the lack of a suitable initial parameter estimate $p^{(0)}$ may lead to a breakdown of the employed NLP solver or that a large number of iterations may be required until the solver terminates. To improve on this situation we propose to employ a homotopy-based globalization strategy. The general idea behind this method is outlined in algorithm 1 and we refer to, e.g., Allgower and Georg (1990) and Deuflhard (2004, chapter 5) for a more detailed treatment of such continuation methods. In our setting, the final goal is to obtain a parameter estimate for the measurements $\eta^{(N)}$ that are the actual (real-world) measurements for which model parameters are sought. The reasoning for this methodology lies in the assumption that the model parameters depend continuously on the measurement data. That is, altering the measurements slightly will also only slightly alter the respective parameter estimates and the employed inverse method will converge quickly. We formalize this idea in section 2.4 where we consider constrained nonlinear least squares (NLLS) problems that are solved with the generalized Gauss–Newton method.

The core question when one wants to apply algorithm 1 is how to generate the sequence of measurements $\{\eta^{(1)}, \dots, \eta^{(N)}\}$. We propose to use EMG functions, as they are known to describe chromatography data well, compare Grushka (1972) and Foley and Dorsey (1984). To this end, we first introduce two versions of such functions; one to describe tailing behavior, and another one to describe fronting behavior, compare figure 2.

Definition 2.2 (Exponentially modified Gaussian functions)**.** Exponentially modified Gaussian (EMG) functions that can be used to describe peaks with fronting behavior ($\mathrm{emg_F}\colon \mathbb{R} \to \mathbb{R}$) and tailing behavior ($\mathrm{emg_T}\colon \mathbb{R} \to \mathbb{R}$) are given by

$$\begin{aligned} \mathrm{emg_T}(t; A, \mu, \sigma, \tau) &= \frac{A\sigma}{\tau}\sqrt{\frac{\pi}{2}} \exp\left(\frac{\sigma^2}{2\tau^2} - \frac{t-\mu}{\tau}\right) \operatorname{erfc}\left(\frac{\sigma}{\sqrt{2}\tau} - \frac{t-\mu}{\sqrt{2}\sigma}\right), \\ \mathrm{emg_F}(t; A, \mu, \sigma, \tau) &= \frac{A\sigma}{\tau}\sqrt{\frac{\pi}{2}} \exp\left(\frac{\sigma^2}{2\tau^2} + \frac{t-\mu}{\tau}\right) \operatorname{erfc}\left(\frac{\sigma}{\sqrt{2}\tau} + \frac{t-\mu}{\sqrt{2}\sigma}\right), \end{aligned} \tag{1}$$

with

$$\operatorname{erfc}(x) = 1 - \operatorname{erf}(x) = \frac{2}{\sqrt{\pi}} \int_x^\infty \exp(-t^2)\,\mathrm{d}t, \qquad x \in \mathbb{R},$$

being the complementary error function. Here, $(A, \mu, \sigma, \tau) \in \mathbb{R}^4$ are parameters specifying the behavior of the respective EMG function.

We first remark that the "classic" EMG function ($\mathrm{emg_T}$) can be interpreted as a scaled probability density function of the sum of a normally distributed and an exponentially distributed random

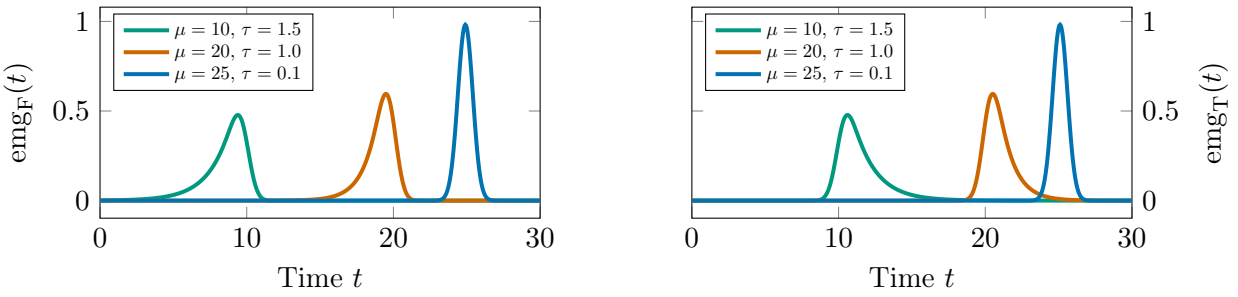

Figure 2: Exemplary EMG functions for peaks with fronting behavior (left) and tailing behavior (right), using (1). All instances are generated with $A = 1.0$ and $\sigma = 0.5$.

variable. The EMG parameters are the amplitude A, the mean μ and standard deviation σ of the underlying Gaussian and the reciprocal of the underlying exponential's rate τ.

To use EMG functions in the context of a moment analysis, compare Schmidt-Traub et al. (2012, section 6.5.3), the following lemma summarizes mean and standard deviation of the EMG functions defined in (1).

Lemma 2.3 (Mean and standard deviation of EMG functions)**.** The mean (μ_{emg}) and standard deviation (σ_{emg}) for the EMG functions defined in (1) are given by

$$\mu_{\mathrm{emg}} = \begin{cases} \mu + \tau, & \text{for } \mathrm{emg_T}, \\ \mu - \tau, & \text{for } \mathrm{emg_F}, \end{cases} \qquad \sigma^2_{\mathrm{emg}} = \sigma^2 + \tau^2.$$

With EMG functions at hand, we can now describe our homotopy approach. The general situation is depicted in figure 3 and an algorithmic description can be found in algorithm 2. The core idea is to both fit the real-world measurements and the model prediction corresponding to the initial parameter estimate $p^{(0)}$ with EMG functions. We thus obtain two sets of EMG parameters; using a convex combination of these two sets of parameters generates intermediate peaks, compare figure 3. In this figure, we can also observe that both the (real-world) measurements and the measurements obtained by using the initial parameter estimate are well approximated by EMG functions. We furthermore highlight that with this approach there will always be only a single peak present in the intermediate stages. This would not be the case, e.g., when using a simple convex combination of the measurement data. In the latter case, we would obtain two peaks in the intermediate steps, which is typically not a physical behavior and a mathematical (mechanistic) model will not be able to capture this.

In order to apply algorithm 2, we need to obtain the EMG parameters $p^{(0)}_{\mathrm{emg}}$ and p^{*}_{emg}. This may also be challenging by itself, as the EMG functions (1) are highly nonlinear. However, depending on the quality of the measurement data, it is possible to obtain good initial estimates based on the first and central second and third moments, as is described in the following lemma.

Lemma 2.4 (Obtaining EMG parameters from (central) moments)**.** Let $\eta \in \{\mathrm{emg_F}, \mathrm{emg_T}\}$ be an instance of an EMG function, either for fronting or tailing behavior. Given the first three (central) moments

$$\mu_1 = \frac{\int_0^\infty t\,\eta(t)\,\mathrm{d}t}{\int_0^\infty \eta(t)\,\mathrm{d}t}, \quad \mu_2 = \frac{\int_0^\infty (t-\mu_1)^2\,\eta(t)\,\mathrm{d}t}{\int_0^\infty \eta(t)\,\mathrm{d}t}, \quad \mu_3 = \frac{\int_0^\infty (t-\mu_1)^3\,\eta(t)\,\mathrm{d}t}{\int_0^\infty \eta(t)\,\mathrm{d}t}, \tag{3}$$

Algorithm 2: Homotopy approach using EMG functions for a single peak.

Input: Model response function h, initial parameter guess $p^{(0)}$, (real-world) measurements η^*, homotopy parameters $0 \leq \lambda^{(1)} \leq \cdots \leq \lambda^{(N)} = 1$ with $N \in \mathbb{N}$.

Output: Parameter estimate p^* for measurements η^*.

1 Obtain "artificial" measurements $\eta^{(0)}$ by using model response function h with parameters $p^{(0)}$.

2 Fit $\eta^{(0)}$ with an EMG function to obtain its parameters $p_{\text{emg}}^{(0)}$ and the corresponding EMG curve denoted by $\eta_{\text{emg}}^{(0)}$.

3 Fit the original (real-world) measurements η^* with the same type (!) of EMG function to obtain $p_{\text{emg}}^{(N)}$ and the corresponding EMG curve $\eta_{\text{emg}}^{(N)}$.

4 **for** $k = 1$ **to** N **do**

5 Compute new EMG parameters, for example, by

$$p_{\text{emg}}^{(k)} = \left(1 - \lambda^{(k)}\right) p_{\text{emg}}^{(0)} + \lambda^{(k)}\, p_{\text{emg}}^{(N)} \tag{2}$$

and compute the corresponding EMG curve $\eta_{\text{emg}}^{(k)}$.

6 Obtain new parameter estimate $p^{(k)}$ based on measurements $\eta_{\text{emg}}^{(k)}$ by applying the chosen inverse method. Use $p^{(k-1)}$ (or a suitable predictor) as initial guess.

7 **end**

8 Use $p^{(N)}$ as initial guess to obtain the parameter estimate p^* for the original measurements η^*.

the EMG parameters for η are given by

$$\tau = \left|\frac{\mu_3}{2}\right|^{1/3}, \quad \sigma = \sqrt{\mu_2 - \tau^2}, \quad \mu = \begin{cases} \mu_1 - \tau, & \text{if } \eta = \text{emg}_{\text{T}}, \\ \mu_1 + \tau, & \text{if } \eta = \text{emg}_{\text{F}}, \end{cases} \quad A = \frac{\int_0^\infty \eta(t)\,\mathrm{d}t}{\sqrt{2\pi\sigma^2}}. \tag{4}$$

Of course, real-world measurements are never perfect EMG functions, hence the above expressions in (4) only serve as rough estimates. The three moments μ_1, μ_2, and μ_3, can be easily computed from the given measurements, e.g., with the trapezoidal rule, provided that the sampling rates of the measurement devices are sufficiently high and the measurement noise low. Otherwise, results obtained for the second and third central moments may be inaccurate, compare Schmidt-Traub et al. (2012, section 6.5.3.1).

Having stated the homotopy algorithm using EMG functions (algorithm 2), as well as how to obtain estimates for EMG parameters based on (central) moments (lemma 2.4), we now draw our attention to possible extensions for the proposed methodology.

2.3. Extensions

Several open questions to the proposed homotopy method remain. First and foremost, the question is whether this approach can also be used when multiple peaks are present. We can generalize the above ideas to the multi-component case by using sums of EMG functions,

$$\eta_{\text{emg}}(t) \coloneqq \sum_{j=1}^{N_f} \text{emg}_{\text{F}}(t; A_j, \mu_j, \sigma_j, \tau_j) + \sum_{j=N_f+1}^{N_f+N_t} \text{emg}_{\text{T}}(t; A_j, \mu_j, \sigma_j, \tau_j).$$

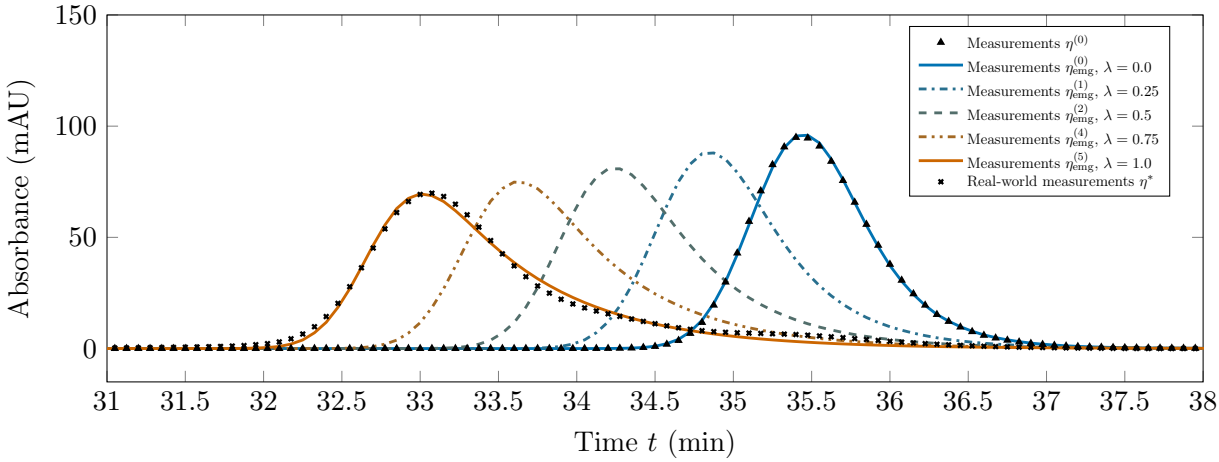

Figure 3: Exemplary visualization of the homotopy approach based on EMG functions, see algorithm 2. The left-most data shows real-world measurements (point data) and the corresponding fit with an EMG function; the right-most data shows "artificial" measurements obtained from evaluating the model response function h using the initial estimate $p^{(0)}$. Intermediate curves show EMG functions obtained via (2).

Here, we assume that the actual measurements consist of N_f peaks with fronting and N_t peaks with tailing behavior. For each component (peak) there is a separate collection of EMG parameters; when using the homotopy approach stated in algorithm 2, the EMG parameters for each component are altered according to (2). Of course, we have to assume that the underlying mathematical model can always describe the current measurement data along the homotopy sufficiently well.

We immediately highlight that peaks not (strongly) overlapping with other peaks can be treated separately when it comes to the estimation of suitable EMG parameters for the respective peak. However, the situation is more difficult when two peaks strongly overlap. First, it might not be obvious whether to use an EMG function with tailing or fronting. Second, even if we can deduce the shape of the peak, we cannot apply (4) to generate good initial guesses for the EMG parameters. In favor of numerical stability, τ should initially be chosen sufficiently large. Furthermore, the mean μ can be roughly obtained by taking the position of the peak maximum. Hence relatively good initial guesses for two out of four parameters are available. A postprocessing of the underlying measurements, where peaks are extrapolated based on their non-overlapping data and subsequently fit by an EMG function, may also work to obtain good initial estimates.

A further remaining question is how to choose the sequence of homotopy steps $\{\lambda^{(k)}\}_{k=1}^{N}$. On the one hand, we prefer a small number of steps N, hence making fast progress. On the other hand, forcing too large steps may again lead to non-convergence of the employed NLP solver. One possibility to determine an efficient sequence of homotopy steps is to use a heuristic based on a discrete proportional-integral controller that monitors a certain contraction factor, compare Potschka and Bock (2021), but also other strategies have been proposed and analyzed, see Allgower and Georg (1990) and Deuflhard (2004, chapter 5). We recapitulate another strategy, due to Bock and coworkers, in section 2.4. In our cases studies, compare section 3.3, we are going to use a rather small fixed step size, as this strategy leads to reliable results and where the employed inverse method typically converges in just few iterations. Furthermore, we always use the previously determined parameter estimate as initial guess, not a more elaborate predictor. This strategy is also known as the classical continuation method.

As a last comment, we remark that if a peak cannot be suitably described by an EMG function, alternatives exist, such as so-called hyper-EMG functions (Purushothaman et al., 2017) that are much more flexible, but also more complex. To conclude, we believe our proposed homotopy approach based on EMG functions to be highly versatile and to cover a wide range of chromatographic applications.

2.4. Traceability of a homotopy when solving NLLS problems with the generalized Gauss–Newton method

To also back up the proposed approach theoretically, we give a brief outline why and when a homotopy approach may lead to a solution of the considered parameter estimation problem, whereas not using such an approach may lead to failure. To this end, we consider an equality-constrained NLLS problem that is solved with a generalized Gauss–Newton method, as is also done in our case study in section 3. We remark that the results shown in this section are primarily attributable to Bock and coworkers (Bock, 1987; Bock et al., 2007) and the following paragraphs shall only serve as a rough overview. An excellent introduction to the subject of continuation methods is given by Allgower and Georg (1990). Furthermore, this subject has also been studied by, e.g., Deuflhard and coworkers, see Deuflhard (2004) and Hohmann (1993) for further details.

We begin our considerations with the statement of the problem class.

Definition 2.5 (Equality-constrained nonlinear least squares problem)**.** Let $F_1 \in \mathcal{C}^1(\mathbb{R}^n, \mathbb{R}^{n_1})$ and $F_2 \in \mathcal{C}^1(\mathbb{R}^n, \mathbb{R}^{n_2})$ with $n_1 \geq n$ and $n_2 < n$. We consider constrained NLLS problems of the form

$$\begin{aligned} \min_{x \in \mathbb{R}^n} \quad & \|F_1(x)\|_2^2 \\ \text{s.t.} \quad & F_2(x) = 0. \end{aligned} \tag{NLLS}$$

We solve (NLLS) with the generalized Gauss–Newton method outlined in the next definition.

Definition 2.6 (Generalized Gauss–Newton method)**.** Let an initial estimate $x^{(0)} \in \mathbb{R}^n$ be given. In the kth iteration the generalized Gauss–Newton method computes a new iterate according to $x^{(k+1)} = x^{(k)} + \alpha^{(k)} \delta x^{(k)}$, where $\alpha^{(k)}$ is a step size from a suitable globalization strategy (see, e.g., Nocedal and Wright, 2006, chapter 3 and section 18.3), and $\delta x^{(k)}$ is a solution of the subproblem

$$\begin{aligned} \delta x^{(k)} = \underset{\delta x \in \mathbb{R}^n}{\arg\min} \quad & \|F_1^{(k)} + J_1^{(k)} \delta x\|_2^2 \\ \text{s.t.} \quad & F_2^{(k)} + J_2^{(k)} \delta x = 0, \end{aligned} \tag{5}$$

where we abbreviate $F_i^{(k)} \coloneqq F_i(x^{(k)})$ and $J_i^{(k)} \coloneqq J_i(x^{(k)})$, the latter being the respective Jacobian matrix for $i \in \{1, 2\}$.

Under certain regularity assumptions, the solution of the subproblem (5) can be expressed via a generalized inverse as introduced in the following theorem.

Theorem 2.7 (Generalized inverse as a solution operator for (5))**.** Let $x \in \mathbb{R}^n$ and furthermore $F = (F_1^T, F_2^T)^T$ and $J = (J_1^T, J_2^T)^T$. Moreover, let

$$\operatorname{rank}(J_2) = n_2, \qquad \operatorname{rank}(J) = n \tag{REG}$$

hold in an open neighborhood $\mathcal{D} = \mathcal{D}(x)$ around x. We then have:

- There exists a mapping $J^+\colon \mathbb{R}^n \to \mathbb{R}^{n\times(n_1+n_2)}$ with $\delta x = -J^+(x)F(x)$, hence $J^+(x)$ is a solution operator for the linearized subproblem (5).
- The mapping J^+ is continuously differentiable for all $y \in \mathcal{D}(x)$.
- The generalized inverse has the form

$$J^+(x) = \begin{pmatrix} I_{n\times n} & 0_{n\times n_2} \end{pmatrix} \begin{pmatrix} J_1(x)^T J_1(x) & J_2(x)^T \\ J_2(x) & 0_{n_2\times n_2} \end{pmatrix}^{-1} \begin{pmatrix} J_1(x)^T & 0_{n\times n_2} \\ 0_{n_2\times n_1} & I_{n_2\times n_2} \end{pmatrix}, \tag{6}$$

  where the subscripts of the zero and identity matrices signify their respective dimensions.

Proof. See Bock (1987, theorem 3.1.31). □

With the concept of the generalized inverse as introduced in theorem 2.7 we can present a result of local convergence due to Bock.

Theorem 2.8 (Local contraction theorem)**.** Let $\mathcal{D} \subseteq \mathbb{R}^n$ be a domain, $F = (F_1^T, F_2^T)^T$, $J = (J_1^T, J_2^T)^T$, and let $J^+\colon \mathcal{D} \to \mathbb{R}^{n\times(n_1+n_2)}$ denote the generalized inverse in the sense of theorem 2.7, assume (REG) holds for all $x \in \mathcal{D}$. For all x, $y \in \mathcal{D}$ with $y = x + \delta x$, where $\delta x = -J^+(x)F(x)$, and for all $t \in [0, 1]$, the following conditions shall be satisfied:

1. There exists $\omega < \infty$ with

$$\left\| J^+(y)\big[J(x + t\,\delta x) - J(x)\big]\delta x \right\| \le \omega\, t \left\|\delta x\right\|^2.$$

2. There exists $\kappa < 1$ with

$$\left\| J^+(y)R(x) \right\| \le \kappa \left\|\delta x\right\|,$$

   where $R(x) = F(x) - J(x)J^+(x)F(x)$ denotes the residual.
3. For an initial guess $x^{(0)}$, the step $\delta x^{(0)} = -J^+(x^{(0)})F(x^{(0)})$ satisfies

$$\delta^{(0)} := \frac{\omega}{2} \left\|\delta x^{(0)}\right\| + \kappa < 1.$$

4. Furthermore, we require $\mathcal{D}^{(0)} \subseteq \mathcal{D}$, where $\mathcal{D}^{(0)} := \overline{\mathcal{B}}\big(x^{(0)}, \frac{\|\delta x^{(0)}\|}{1-\delta^{(0)}}\big)$ is the closed ball around $x^{(0)}$ with radius $\frac{\|\delta x^{(0)}\|}{(1-\delta^{(0)})}$.

Then the following holds:

- The sequence of iterates generated by the generalized Gauss–Newton method with full steps $\alpha^{(k)} \equiv 1$ remains in $\mathcal{D}^{(0)}$.
- There exists $x^* \in \mathcal{D}^{(0)}$ with

$$x^{(k)} \overset{k\to\infty}{\longrightarrow} x^* \qquad \text{and} \qquad J^+(x^*)F(x^*) = 0,$$

  i.e., x^* is a fixed point.

Proof. See Bock (1987, theorem 3.1.44). □

Two remarks are in order: First of all, the prerequisites of theorem 2.8, particularly those involving ω and κ, have to hold for an arbitrary, selectable norm. For the unconstrained case, one can show that if $\kappa > 1$ for any norm then there exists a perturbation of x^* such that the generalized Gauss–Newton iterations move away from x^*. Furthermore, it can be shown that a minimum x^* with $\kappa(x^*) > 1$ is not even desired, as it is not statistically stable for the measurements. For further details, we refer to Bock et al. (2020) and the references cited therein.

Secondly, the critical condition to fulfill is indeed $\kappa < 1$. This can be achieved, e.g., if the residual R is small in the vicinity of a solution. The main motivation for a homotopy approach is to ensure that this property (a small residual) is satisfied when using a previously computed solution as an initial guess for the next problem instance along the homotopy.

The reasoning for local convergence along the homotopy goes as follows: Let the prerequisites of theorem 2.8 be satisfied for a specific problem instance and assume that for each instance along the homotopy a unique solution exists. Then, as long as the homotopy step is not too large, if the previously computed solution lies in the area of contraction $\mathcal{D}^{(0)}$ of the current problem instance, we can expect convergence to the next solution along the homotopy, whose existence can be backed up by the implicit function theorem.

We want to formalize this reasoning in a concise manner. To this end, we first have to extend the setting for constrained NLLS problems.

Definition 2.9 (Embedded equality-constrained nonlinear least squares problem)**.** Let, w.l.o.g., $I := [0, 1]$. Let $F_1 \in \mathcal{C}^2(\mathcal{D} \times I, \mathbb{R}^{n_1})$ and $F_2 \in \mathcal{C}^2(\mathcal{D} \times I, \mathbb{R}^{n_2})$, with a domain $\mathcal{D} \subseteq \mathbb{R}^n$, $n_1 \geq n$ and $n_2 < n$. For a homotopy parameter $\lambda \in I$ we consider embedded constrained NLLS problem of the form

$$\begin{aligned} \min_{x \in \mathbb{R}^n} \quad & \|F_1(x, \lambda)\|_2^2 \\ \text{s.t.} \quad & F_2(x, \lambda) = 0. \end{aligned} \tag{NLLS(λ)}$$

In our case, compare section 2, the homotopy parameter λ describes the sequence of measurements generated by the EMG functions. For $\lambda = 0$ we assume that a solution is known and we are interested in a solution for $\lambda = 1$, also compare algorithm 2. For the remainder of this section, we have to agree on the following assumption.

Assumption 2.10. For all $\lambda \in I$ we assume that there exists a unique solution $x = x(\lambda)$ for (NLLS(λ)). We furthermore assume that $x \colon I \to \mathbb{R}^n$ is continuous.

We note that the continuity property can also be deduced by (repeated) application of the implicit function theorem, when assuming the regularity condition (REG) in theorem 2.12.

The idea in algorithms 1 and 2 is that a previously computed parameter estimate is used as an initial guess for the successive problem instance along the homotopy. We can formalize and generalize this idea by means of a predictor P with a growth function W.

Definition 2.11 (Predictor with growth function)**.** We call a mapping $P \colon I \to \mathbb{R}^n$ predictor with growth function W in $\widehat{\lambda} \in I$, if there exists $\widetilde{\eta} > 0$ such that

$$\|P(\widehat{\lambda} + h) - x(\widehat{\lambda} + h)\| \leq \widetilde{\eta} W(h), \quad \widehat{\lambda} \leq \widehat{\lambda} + h \in I$$

holds. Here, we call a function $W \colon \mathbb{R}_{\geq 0} \to \mathbb{R}_{\geq 0}$ a growth function (also known as class $\mathcal{K}$ function) if it is continuous, strictly increasing, and $W(0) = 0$.

We remark that simply using the previous computed solution as initial guess for the successive problem corresponds to using the predictor $P(\widehat{\lambda}+h) = x(\widehat{\lambda})$ with growth function $W(h) = h$ and factor $\widetilde{\eta}$, provided that the solution trajectory $x(\cdot)$ is Lipschitz continuous on I with Lipschitz constant $\widetilde{\eta}$.

With this setup we can now present a result of local convergence along the homotopy.

Theorem 2.12. For all $\lambda \in I$, let $x(\lambda)$ be the unique solution of (NLLS(λ)), compare assumption 2.10, with $x(\lambda) \in \mathcal{D}(\lambda)$, where $\mathcal{D}(\lambda)$ is a convex domain. Let $\widehat{\mathcal{D}} \supseteq \{(x,\lambda) \mid \lambda \in I, x \in \mathcal{D}(\lambda)\}$ be a domain, $F = (F_1^T, F_2^T)^T \in \mathcal{C}^2(\widehat{\mathcal{D}}, \mathbb{R}^{n_1+n_2})$, and $J = (J_1^T, J_2^T)^T$ denote the Jacobian of F with respect to x. For all $(x,\lambda) \in \widehat{\mathcal{D}}$ we assume that a generalized inverse $J^+(x,\lambda)$ in the sense of theorem 2.7 exists. Moreover, for all $\lambda \in I$, $s \in [0,1]$, $x, y \in \mathcal{D}(\lambda)$ the following conditions shall be satisfied:

1. There exists $\omega < \infty$ with
$$\left\| J^+(y,\lambda)\big[J(x+s\,(y-x),\lambda) - J(x,\lambda)\big](y-x)\right\| \leq \omega\, s \left\|y-x\right\|^2.$$
2. There exists $\kappa < 1$ with
$$\left\| J^+(y,\lambda) R(x,\lambda)\right\| \leq \kappa \left\|y-x\right\|,$$
where $R(x,\lambda) = F(x,\lambda) - J(x,\lambda)J^+(x,\lambda)F(x,\lambda)$ denotes the residual.
3. Let a predictor P with growth function W be given such that (2.11) holds for fixed $\widetilde{\eta} > 0$ that is independent of $\lambda \in I$.
4. For a chosen, but fixed $\delta < 1$ with $\kappa < \delta$ and $\gamma := \kappa + 1$ let
$$h_{\max} := \min\left(W^{-1}\left(\frac{\gamma(\sqrt{1+4(\delta-\kappa)\ \gamma^2}-1)}{\omega\widetilde{\eta}}\right), 1-\lambda\right). \tag{7}$$
We then require for all $h \in [0, h_{\max}]$ that $\widetilde{\mathcal{B}} := \overline{\mathcal{B}}\big(\widetilde{x}, \frac{\widetilde{a}}{1-\delta}\big) \subseteq \mathcal{D}(\widetilde{\lambda})$, where $\widetilde{\lambda} := \lambda + h$, $\widetilde{x} := P(\widetilde{\lambda})$, and $\widetilde{a} := \|J^+(\widetilde{x},\widetilde{\lambda})F(\widetilde{x},\widetilde{\lambda})\|$.

Then, for all $\widetilde{\lambda} \in [\lambda, \lambda + h_{\max}]$ the sequence of iterates generated by the generalized Gauss–Newton method using the initial guess $x^{(0)} := P(\widetilde{\lambda})$ and with full steps $\alpha^{(k)} \equiv 1$ remains in $\widetilde{\mathcal{B}}$ and converges to $x(\widetilde{\lambda})$.

Proof. See Bock (1987, theorem 3.3.20). There, one can also find further a priori estimates, which do not, however, play a role in our context. □

We first remark that for the specific NLLS problems used in our case studies, compare (9), only the measurements are dependent on the homotopy parameter λ, as they are altered along the homotopy. Hence, the Jacobians with respect to the unknowns and also the generalized inverse are independent of λ. Therefore, condition 1 in theorem 2.12 is not much more restricitve than its counterpart in theorem 2.8.

We furthermore note that although theorem 2.12 gives us specific values for a maximum step size along the homotopy, it is difficult to apply this result in practice, as the Lipschitz constants ω and κ, as well as $\widetilde{\eta}$ are difficult to obtain. Lower bounds for these constants can be obtained, e.g., by sampling the domain $\mathcal{D}$, but of course this is computationally expensive. Nonetheless, the presented results serve as a theoretical underpinning.

3. Model calibration for a real-world IEX process

In this section, we put the proposed homotopy approach presented in section 2 into practice by considering a real-world IEX process. We first introduce the experimental setup, including the employed mathematical models, followed by a detailed description of the methodology to estimate all model parameters, with an emphasis on the application of our novel homotopy approach.

3.1. Experimental setup

We briefly describe the experimental setup, as well as the employed mathematical models and our numerical solution strategy for nonlinear least squares problems constrained by (ordinary and partial) differential equations. We remark that the experimental setup and the employed mathematical models, see sections 3.1.1 and 3.1.2, are the same as in one of our previous publications (Cebulla et al., 2023). However, for the sake of completeness and better understanding, we briefly restate the most important aspects and refer the reader to said publication for further details.

3.1.1. Apparatus, chromatography column, chemical substances

For chromatographic experiments, we use an ÄKTA$^{\text{TM}}$ pure 150 chromatography system in combination with a UV monitor U9-M with 0.2 cm optical path length, as well as a conductivity monitor C9n. A Tricorn$^{\text{TM}}$ 5/50 chromatography column is used, whose height is shortened to 25 mm by adjusting the height of the movable adapter, thus having an approximate column volume of 0.5 mL. The ion exchanger is a Capto$^{\text{TM}}$ Q ImpRes strong anion exchanger. All of the aforementioned equipment is purchased from Cytiva (Marlborough, MA, USA). Buffer components such as sodium chloride, tris, and sodium hydroxide, are purchased from Merck KGaA (Darmstadt, Germany).

We examine two substances: The product is VWF-12 (Octapharma Biopharmaceuticals GmbH, Heidelberg, Germany), which is a recombinant dimeric fragment of the so-called von Willebrand factor. This substance aims to prolong the half-life of proteins, such as factor VIII (Kannicht et al., 2017; Vollack-Hesse et al., 2021). As an impurity we use HSA (human serum albumin; Sigma–Aldrich, St. Louis, MO, USA), which has a similar isoelectric point as VWF-12 (HSA: 4.7, VWF-12: 4.83). It can thus bind to the ion exchanger at the same buffer pH.

3.1.2. Mathematical models

To mathematically describe the IEX process, we employ a so-called transport-dispersive model (TDM), compare (Schmidt-Traub et al., 2012, section 6.2.5.1), in combination with a kinetic version of the SMA isotherm model (Brooks and Cramer, 1992), as this is a widely accepted model to describe the adsorption behavior in IEX.

The model describes the concentration profiles of all components i along the axial position $x \in (0, L_c)$ of the column for a given time $t \in (0, t_f)$,

$$\frac{\partial c_{m,i}}{\partial t}(t,x) = -\frac{v_{\text{sup}}}{\varepsilon_b}\frac{\partial c_{m,i}}{\partial x}(t,x) + D_{\text{ax}}\frac{\partial^2 c_{m,i}}{\partial x^2}(t,x) - \frac{1-\varepsilon_b}{\varepsilon_b}\frac{3}{r_p}k_{\text{eff},i}\left(c_{m,i}(t,x) - c_{p,i}(t,x)\right), \tag{8a}$$

$$\frac{\partial c_{p,i}}{\partial t}(t,x) = -\frac{1-\varepsilon_p}{\varepsilon_p}\frac{\partial q_i}{\partial t}(t,x) + \frac{3}{\varepsilon_p r_p}k_{\text{eff},i}\left(c_{m,i}(t,x) - c_{p,i}(t,x)\right), \tag{8b}$$

$$\frac{\partial q_i}{\partial t}(t,x) = k_{\text{ads},i}\Big(\Lambda_{\text{IEX}} - \sum\nolimits_{j=1}^{n_{\text{comp}}}\left(z_{\text{p},j} + \varsigma_j\right)q_j(t,x)\Big)^{z_{\text{p},i}} c_{p,i} - k_{\text{des},i}c_{p,\text{salt}}^{z_{\text{p},i}}\, q_i(t,x), \tag{8c}$$

$$\frac{\partial q_{\text{salt}}}{\partial t}(t,x) = -\sum\nolimits_{j=1}^{n_{\text{comp}}} z_{\text{p},j}\,\frac{\partial q_j}{\partial t}(t,x). \tag{8d}$$

Here, (8a) and (8b) hold for all $i \in \{1, \dots, n_{\text{comp}}\} \cup \{\text{salt}\}$, whereas (8c) holds for $i \in \{1, \dots, n_{\text{comp}}\}$.

The states in the TDM (8) are the concentrations in the mobile phase $c_{m,i}$, the liquid particle phase $c_{p,i}$, and the adsorbed phase q_i. Except for the (here fixed) superficial flow velocity v_{sup}, all further quantities in (8) are model parameters. The actual adsorption kinetics are given by (8c) for a "normal" (protein) component and by (8d) for a salt (or modifier) component that affects the adsorption behavior of the other components.

The TDM (8) is completed with Danckwerts' boundary conditions (Danckwerts, 1953), which are given by

$$\frac{\partial c_{m,i}}{\partial x}(t,0) = \frac{v_{\text{sup}}}{\varepsilon_b D_{\text{ax}}} \left(c_{m,i}(t,0) - c_{\text{in},i}(t)\right), \quad \frac{\partial c_{m,i}}{\partial x}(t,L_c) = 0,$$

for $i \in \{1, \dots, n_{\text{comp}}\} \cup \{\text{salt}\}$ and $t \in [0, t_f]$. Here, $c_{\text{in},i}$ is the inlet concentration of component i, a time-dependent control degree of freedom.

The initial values correspond to an equilibrated column and we thus have for $x \in [0, L_c]$

$$\begin{aligned} &c_{m,i}(0,x) = 0, && c_{p,i}(0,x) = 0, && q_i(0,x) = 0, && \text{for } i \in \{1, \dots, n_{\text{comp}}\}, \\ &c_{m,\text{salt}}(0,x) = c_{\text{salt,init}}, && c_{p,\text{salt}}(0,x) = c_{\text{salt,init}}, && q_{\text{salt}}(0,x) = \Lambda_{\text{IEX}}. \end{aligned}$$

As the dead volume (or extracolumn volume) is approximately five times larger than the column volume, we additionally take tubing, mixing chambers, and detectors of the chromatography system into account. We model mixing chambers and detectors with a continuous stirred tank (CST) model that is given by the initial value problem

$$\frac{\mathrm{d}c_i^{\text{cst}}}{\mathrm{d}t}(t) = \frac{\dot{V}}{V^{\text{cst}}}\Big(c_{\text{in},i}^{\text{cst}}(t) - c_i^{\text{cst}}(t)\Big), \qquad c_i^{\text{cst}}(0) = c_{\text{init},i}^{\text{cst}}.$$

Additional tubing with length $L^{\text{dpf}} > 0$ is modeled by a dispersed plug flow (DPF) model given by

$$\frac{\partial c_i^{\text{dpf}}}{\partial t}(t,x) = -v^{\text{dpf}} \frac{\partial c_i^{\text{dpf}}}{\partial x}(t,x) + D_{\text{ax}}^{\text{dpf}} \frac{\partial^2 c_i^{\text{dpf}}}{\partial x^2}(t,x).$$

Analogously to the TDM (8) the DPF model is completed with Danckwerts' boundary conditions, hence

$$\frac{\partial c_i^{\text{dpf}}}{\partial x}(t,0) = \frac{v^{\text{dpf}}}{D_{\text{ax}}^{\text{dpf}}}\Big(c_i^{\text{dpf}}(t,0) - c_{\text{in},i}^{\text{dpf}}(t)\Big), \quad \frac{\partial c_i^{\text{dpf}}}{\partial x}(t,L^{\text{dpf}}) = 0, \quad c_i^{\text{dpf}}(0,x) = c_{\text{init},i}^{\text{dpf}},$$

for $t \in [0, t_f]$ and initial values for $x \in [0, L_c]$.

With this, all employed models are introduced. In figure 4 we depict the actual modeling of the whole chromatography system, where the outlet concentration of a model is used as an inlet concentration for the respective successive model.

3.1.3. Parameter estimation problem and numerical solution strategy

In order to estimate model parameters based on given measurement data, we solve NLLS problems of the form

$$\begin{aligned} \min_{p, w^{(1)}, \dots, w^{(n_{\text{exp}})}} F_1(p, w^{(1)}, \dots, w^{(n_{\text{exp}})}) &= \sum_{k=1}^{n_{\text{exp}}} \sum_{i=1}^{n_{\text{meas}}^{(k)}} \left(\frac{h^{(k)}(t_i^{(k)}, p;\, w^{(k)}) - \eta_i^{(k)}}{\sigma_i^{(k)}} \right)^2 \\ \text{s.t.} \quad F_2^{(k)}(p, w^{(k)}) &= 0, \quad k \in \{1, \dots, n_{\text{exp}}\}. \end{aligned} \tag{9}$$

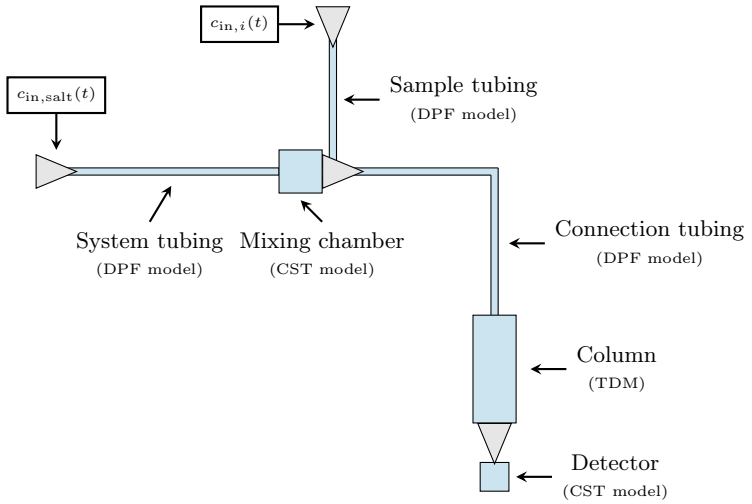

Figure 4: Schematic depiction of the employed chromatography system model.

That is, we consider n_{exp} experiments *simultaneously*, each (potentially) with its own model response function $h^{(k)}$ and independent set of variables $w^{(k)} \in \mathbb{R}^{n_w^{(k)}}$, measurements $\eta^{(k)}$ and standard deviation of measurement noise $\sigma^{(k)}$, but with the same set of parameters p. Additional equality constraints $F_2^{(k)} \colon \mathbb{R}^{n_p+n_w^{(k)}} \to \mathbb{R}^{n_2^{(k)}}$, e.g., discretized ordinary differential equation (ODE) or PDE models, are imposed, each with their own variables $w^{(k)}$, but again with the same parameters p. This formulation corresponds to a maximum likelihood approach when assuming additive measurement noise that is normally distributed with zero mean and known variances $(\sigma_i^{(k)})^2$.

In our case the model response functions describe a linear relationship between outflow concentration c_{out} ($= c_{\text{detector}}^{\text{cst}}$ in our case study) and UV absorption, or conductivity, respectively. For UV absorption, the Lambert–Beer law states that

$$A^{(\lambda)} = \ell_{\text{cp}} \sum_{i=1}^{N} \varepsilon_i^{(\lambda)} c_{\text{out},i}. \tag{10}$$

Here, $A^{(\lambda)}$ is the UV absorption at a specific wavelength λ, our model response. Moreover, ℓ_{cp} is the cell path length of the measurement device, and $\varepsilon^{(\lambda)}$ is a component-dependent attenuation coefficient that we must estimate.

We briefly summarize the most important steps for the numerical solution of (9). We pursue a direct "first discretize, then optimize" approach: First, the PDE models (TDM and DPF models) are spatially semi-discretized, in our case with a higher-order finite volume scheme. The resulting NLLS problem, now solely constrained by ODEs, is then discretized with the direct multiple shooting method, compare Bock and Plitt (1984). The obtained large-scale finite-dimensional NLLS problem is then solved with a structure exploiting variant of the generalized Gauss–Newton method, see Bock (1987), Schlöder (1988), Bock et al. (2007), and Cebulla et al. (2019).

In addition to the advantages of the generalized Gauss–Newton method stated in section 2.4, a covariance matrix $\mathbf{V} \in \mathbb{R}^{n_p \times n_p}$ of the obtained parameter estimates can be cheaply computed when using this method. For details we refer to, e.g., Bock et al. (2007, section 4). We then can use the covariance matrix for computing $(1-\alpha) \cdot 100\%$ confidence intervals: We follow a frequentist

perspective, thus assuming that there exist true, but unknown parameters p^{true}. Having obtained a parameter estimate p^* with the generalized Gauss–Newton method (and additional estimates for the variables w^*), we compute confidence intervals for the ith component via

$$\Pr\left[p_i^{\text{true}} \in \left[p_i^* - t_\ell(1-\alpha)\cdot\sigma_0^*\cdot\sqrt{\mathbf{V}_{ii}},\, p_i^* + t_\ell(1-\alpha)\cdot\sigma_0^*\cdot\sqrt{\mathbf{V}_{ii}}\right]\right] = 1-\alpha, \tag{11}$$

compare, e.g., Smith (2013, Chapters 4 and 7). Here,

$$(\sigma_0^*)^2 = \frac{\|F_1(p^*, w^*)\|_2^2}{\ell}$$

is an estimate for the (unknown) common factor of the variance,

$$\ell = \sum\nolimits_{k=1}^{n_{\text{exp}}} \left(n_{\text{meas}}^{(k)} + n_2^{(k)} - n_w^{(k)}\right) - n_p$$

is the number of degrees of freedom, and $t_\ell(\,\cdot\,)$ denotes the quantile function of the t-distribution with ℓ degrees of freedom and used for two-sided (confidence) intervals. We remark that other strategies to quantify uncertainty are also possible, e.g., by means of a bootstrap method (Borg et al., 2012).

3.2. Separate determination and estimation of model parameters

As already discussed previously, a simultaneous estimation of too many model parameters can lead to meaningless results. It is hence crucial to determine as many parameters as possible separately. In this section, we give a brief description on how we obtain parameters for extra column equipment and selected column and component parameters.

3.2.1. Extra column equipment

By replacing the chromatography column with a zero-volume connector, parts of the flow path of the modeled chromatography system, compare figure 4, can be investigated independently. We perform tracer experiments as described by Schmidt-Traub et al. (2012, section 6.5.2) with two different injected volumes and estimate the model parameters of the combined mathematical models by solving a least squares problem of the form (9) with the generalized Gauss–Newton method. All tracer experiments are performed with a fixed volumetric flow rate $\dot{V} = 0.5\,\text{mL}\,\text{min}^{-1}$, but with different injection volumes V_{inj}. The tracer substance is NaCl and the only measurement device is the conductivity monitor.

We first estimate model parameters for the connection tubing and the successive detector, see figure 4, thus connecting a DPF model for tubing with a CST model for the detector. The experimental data, as well as our obtained fit, are depicted in figure 5; values and confidence intervals are summarized in table 3.

To estimate the model parameters for the system tubing and mixing chamber, we add a DPF and CST model to the mathematical model used before and keep the previously estimated parameters for connection tubing and detector fixed. We depict the data of the corresponding tracer experiments and the optimized model predictions in figure 6, the actual parameter values and confidence intervals are stated in table 3. We highlight that the estimated parameters of the whole flow path correspond to a volume of approximately 2.68 mL, which is more than five times the volume of the employed chromatography column. This makes the calibration even more challenging.

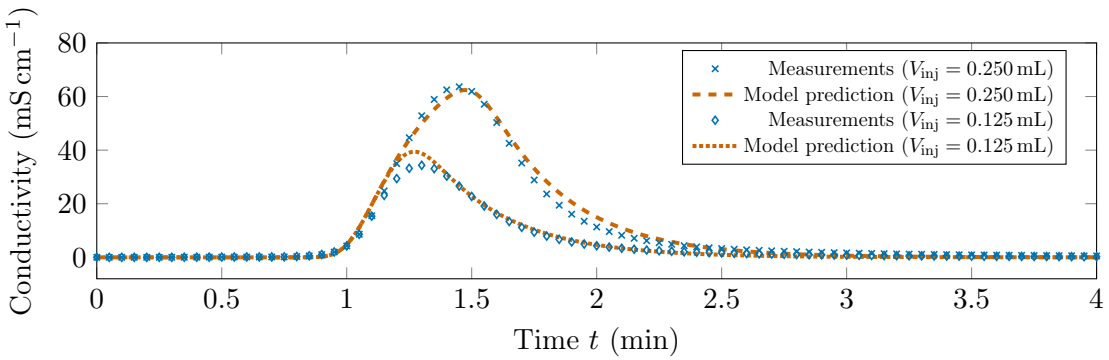

Figure 5: Data of two tracer experiments for the estimation of model parameters of the connection tubing and detector, see figure 4.

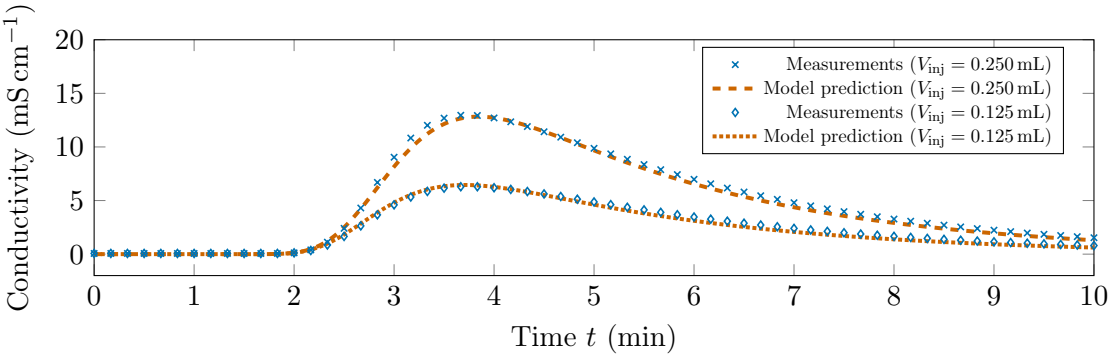

Figure 6: Data of two tracer experiments for the estimation of model parameters of the system tubing and mixing chamber, compare figure 4.

For the sample tubing we use the same factor for axial dispersion as for the system tubing, since both tubings have the same inner diameter. The total volume of the sample tubing is approximately 1.26 mL, which we can convert into a tubing length of roughly 160.4 cm.

We conclude this section with the following remark: We observe that the experimental data, see figures 5 and 6, already shows a considerable amount of tailing. This is noteworthy, as no chromatography column is present in these experiments. We will furthermore see, compare figure 7, that the column itself does indeed only contribute little to peak broadening. It is hence particularly the tubing and measurement devices that seem to be primarily responsible for peak broadening and tailing in our experimental setup.

3.2.2. Column parameters and selected substance parameters

We perform tracer experiments with a moment analysis as described by Schmidt-Traub et al. (2012, section 6.5.3); the measurement data, as well as the corresponding fits with EMG functions, are shown in figure 7.

As a pore entering substance we use NaCl; performing a moment analysis and taking the arithmetic mean of the respective first moments, we obtain a *total* porosity of $\varepsilon_t \approx 0.876$. As we could not find a tracer substance that does *not* enter the pores and hence does not get adsorbed, we use a bed porosity of $\varepsilon_b = 0.37$, which serves as a valid, yet rough approximation (Schmidt-Traub

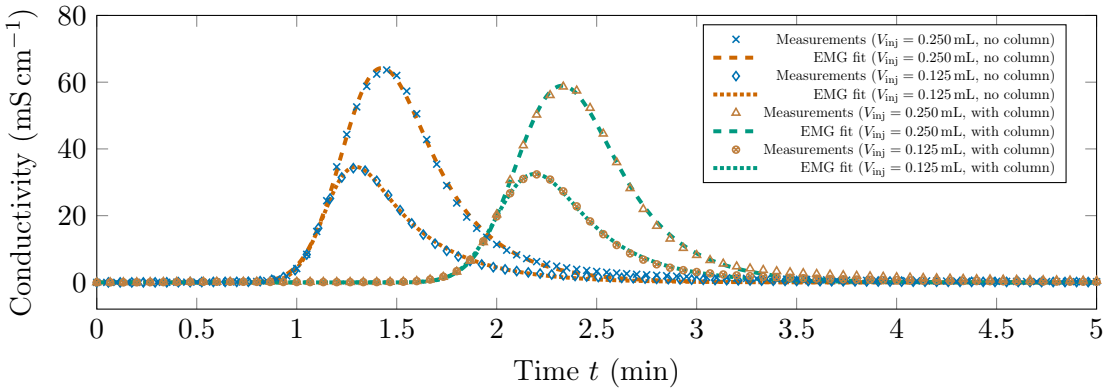

Figure 7: Measurements from different tracer experiments and their corresponding fits using EMG functions.

et al., 2012, page 15). We then compute the particle porosity ε_p via

$$\varepsilon_p = \frac{\varepsilon_t - \varepsilon_b}{1 - \varepsilon_b} = \frac{0.876 - 0.37}{1 - 0.37} \approx 0.80. \tag{12}$$

The ionic capacity is obtained by performing titration experiments (data not shown) as described by Hahn et al. (2016). We obtain an ionic capacity of approximately 0.17 M, which lies within the range 0.15 M – 0.18 M given by the manufacturer.

The particle radius r_p of the resin is taken from manufacturer data. Together with the known molecular weights for VWF-12 ($\mathrm{MW}_{\text{VWF-12}} = 124\,170\,\mathrm{Da}$) and HSA ($\mathrm{MW}_{\text{HSA}} = 69\,084\,\mathrm{Da}$), we can use a correlation to determine the component-dependent mass transfer coefficients, namely

$$k_{\text{eff},i} \approx k_{\text{pore},i} = \frac{5}{r_p} \frac{\varepsilon_p^3}{(2-\varepsilon_p)^2} \frac{1.644 \times 10^{-3}}{\mathrm{MW}_i^{1/3}} \approx \begin{cases} 3.56 \times 10^{-2}\,\mathrm{cm\,min^{-1}} & i = \text{HSA}, \\ 2.93 \times 10^{-2}\,\mathrm{cm\,min^{-1}} & i = \text{VWF-12}. \end{cases} \tag{13}$$

Here, we use a correlation proposed by Polson (1950) to obtain the molecular diffusion coefficients, combined with the Mackie–Meares correlation as stated by Guiochon et al. (2006, eq. 5.76) to obtain the intraparticle pore diffusion coefficient. We compute the rate-limiting intraparticle transport coefficient k_{pore} with a correlation stated by Schmidt-Traub et al. (2012, eq. 6.199). The effective mass transfer coefficient for NaCl is set to $k_{\text{eff,salt}} = 0.15\,\mathrm{cm\,min^{-1}}$, hence NaCl switches between mobile and particle phase sufficiently fast.

Lastly, we determine estimates for the molar attenuation coefficients for 280 nm wavelength, i.e., $\varepsilon_{\text{HSA}}^{(280)}$ and $\varepsilon_{\text{VWF-12}}^{(280)}$, in order to be able to compute the desired model prediction via application of the Lambert–Beer law, compare (10). To this end, UV absorbances are measured for several concentrations and we fit a linear function to the obtained measurements (data not shown). The obtained values are reported in table 3.

3.3. Homotopy approach for estimation of remaining model parameters

Having estimated most model parameters of the chromatography system by the previously described methodology, we now present how to obtain the remaining, primarily adsorption-related parameters by application of the homotopy approach described in section 2.

More specifically, we aim to estimate the following model parameters: the sample concentration $c_{\text{load},i}$ (as the components are not 100% pure), the adsorption rate $k_{\text{ads},i}$, the binding charge $z_{\text{p},i}$,

Table 1: The different phases in bind-and-elute experiments performed to obtain real-world data for the IEX separation process.

Phase	Buffer	Duration	Flow rate $\dot{V}$
1: Equilibration phase	Equilibration buffer (0.1 M NaCl, 0.05 M Tris-HCl, pH 8)	—	$0.5\,\mathrm{mL\,min^{-1}}$
2: Sample injection phase	Equilibration buffer	20 min	$0.5\,\mathrm{mL\,min^{-1}}$
3: CAB phase	Equilibration buffer	5 min	$0.5\,\mathrm{mL\,min^{-1}}$
4: Elution phase 1	Equilibration + elution buffer (0.1 M – 1.0 M NaCl, 0.05 M Tris-HCl, pH 8)	various	$0.5\,\mathrm{mL\,min^{-1}}$
5: Elution phase 2	Elution buffer (1.0 M NaCl, 0.05 M Tris-HCl, pH 8)	5 min	$0.5\,\mathrm{mL\,min^{-1}}$
6: CIP phase	CIP buffer (2.0 M NaCl, 1.0 M NaOH)	5 min	$0.5\,\mathrm{mL\,min^{-1}}$

the shielding parameter ς_i, and the detector volume $V_{\text{detector}}^{\text{cst}}$, as we used a different detector in section 3.2.1, for $i \in \{\text{VWF-12}, \text{HSA}\}$. We choose to fix the desorption parameter for both substances to $k_{\text{des},i} = 1.00 \times 10^8\,\mathrm{M}^{-z_{\text{p},i}}\,\mathrm{min}^{-1}$, as otherwise no meaningful parameter estimates can be obtained (due to high correlations). Nonetheless, the chosen value reflects a fast desorption rate which is often a reasonable assumption. As initial parameter guess to start the homotopy we use, neglecting units,

$$\begin{aligned} &\text{VWF-12}: \quad c_{\text{load}} = 8.05 \times 10^{-7}, \quad k_{\text{ads}} = 1000, \quad z_{\text{p}} = 10, \quad \varsigma = 75, \quad V_{\text{detector}}^{\text{cst}} = 0.157, \\ &\text{HSA}: \quad\quad c_{\text{load}} = 1.45 \times 10^{-6}, \quad k_{\text{ads}} = 1000, \quad z_{\text{p}} = 9, \quad\ \varsigma = 75, \quad V_{\text{detector}}^{\text{cst}} = 0.157. \end{aligned} \tag{14}$$

As measurement data, we have access to four bind-and-elute experiments per substance that are evaluated simultaneously, compare (9). The general steps in each experiment are summarized in table 1; for calibration the CIP phase is not considered. For the elution phase 1 we perform linear salt gradients with 20 min duration (experiments 01 and 02), 30 min duration (experiment 03), and 40 min duration (experiment 04), respectively; for experiment 02 we use a doubled sample concentration compared to the other experiments.

We then follow the steps described in algorithm 2. That is, we fit an EMG function to each experimental data and to each simulated peak obtained with the initial parameter guess, respectively. We then perform the homotopy with *fixed* step sizes of $\Delta\lambda = 0.05$. This value is admittedly rather small, but in most cases the generalized Gauss–Newton method will often converge within just a couple of iterations, with just few, yet notable exceptions. The parameter estimates obtained for $\lambda = 1$ are then used as initial guess for the original measurements. Lastly, we limit the number of iterations taken by the generalized Gauss–Newton method to 15. On the one hand, we can thus ensure that we do not spend too much time in computing a solution for a given homotopy step. On the other hand, the iteration limit is sufficiently large such that for most homotopy instances convergence is well achieved. The standard deviations in the least squares objective function (9) are set to one.

EMG fits for the real-world experiments, as well as for the model predictions obtained with the initial parameter guess, are depicted in figure 8, both for VWF-12 and HSA. The corresponding EMG parameters are summarized in table 2.

We can see that in all cases, the measurements/predictions can be well described by EMG functions, which underlines their capability of describing chromatography data well. We highlight that although the conceptual goal (shifting the peaks to the left) is simple to grasp, the residuals

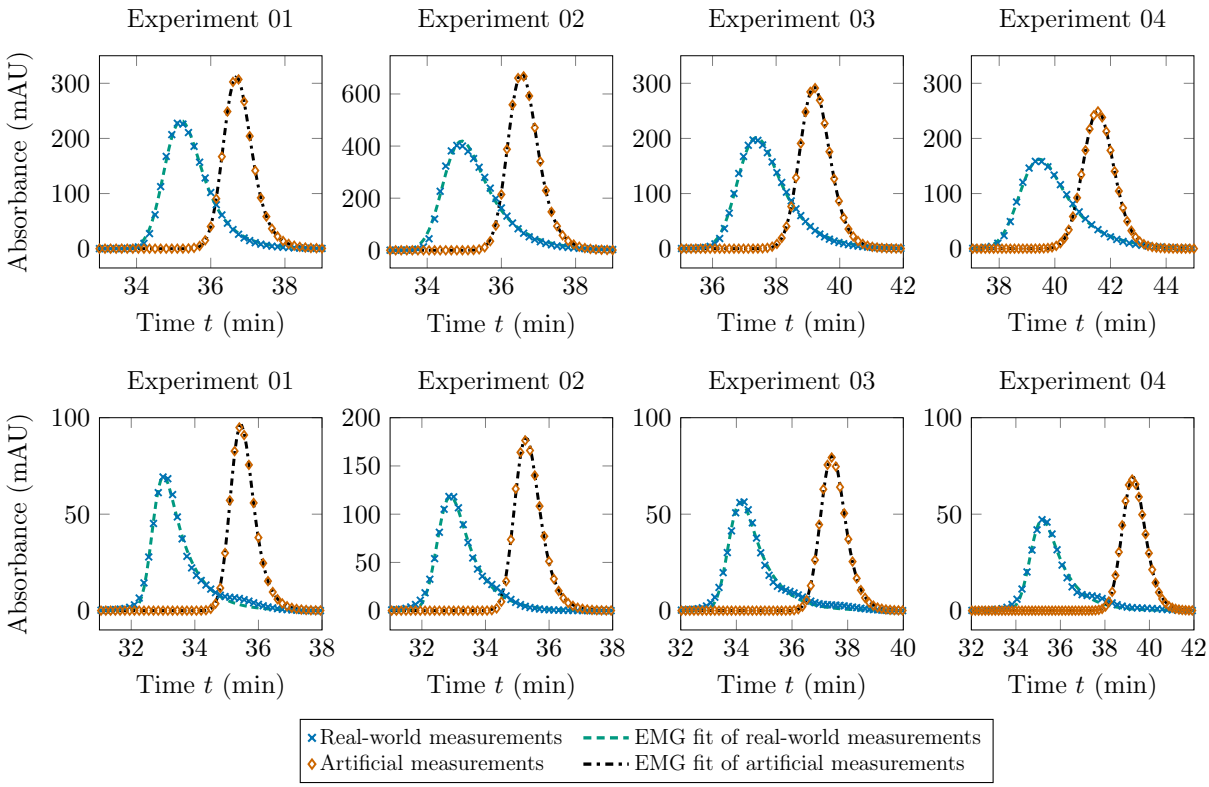

Figure 8: Real-world measurements and artificial measurements, the latter obtained from evaluating the model response with the initial parameter guesses, compare (14) and table 3, as well as the corresponding fits using EMG functions. Top: VWF-12, bottom: HSA.

between real-world data and initial model prediction are very large, which negatively affects the convergence behavior of the generalized Gauss–Newton method, compare section 2.4. Using the homotopy approach aims to counteract against this undesired behavior by generating artificial measurements such that the respective residuals are much smaller.

We first draw our attention to the parameter values along the homotopy path, as some interesting observations can be made. The results are depicted in figure 9.

First, for λ between 0.25 and 0.30, we can observe kinks both for VWF-12 and HSA. This is attributable to the fact that the generalized Gauss–Newton method did not converge within the prescribed iteration limit in these cases, also compare figure 10. Nonetheless, it is remarkable that despite this behavior, we can still perform the homotopy approach until the end. That is, at least for these specific instances, convergence of the generalized Gauss–Newton method is not always necessary to pursue the complete homotopy. This also justifies the choice of a low iteration limit. We note, however, that the generalized Gauss–Newton method would have converged in all cases within 50 iterations.

Furthermore, particularly the parameters k_{ads} and z_{p} vary strongly during the first steps of the homotopy, hence we in fact did start far from a solution. Moreover, it seems that these parameters exhibit a high nonlinearity manifesting as "kinks" in the measurement data. This again is challenging for optimization algorithms. Furthermore, using a more elaborate predictor at these steps on the homotopy, e.g., based on higher-order extrapolation, will typically lead to worse initial guesses

Table 2: EMG parameters for real-world data and for artificial measurements obtained by using the respective initial parameter guess, compare (14) and table 3. The corresponding peaks are depicted in figure 8.

Experiment	Real-world measurements				Initial parameter guess			
	A	μ	σ	τ	A	μ	σ	τ
01 (VWF-12)	352.03	34.862	0.3719	0.5946	401.74	36.474	0.3031	0.3136
02 (VWF-12)	703.99	34.528	0.3923	0.7844	876.50	36.318	0.3198	0.3291
03 (VWF-12)	316.92	36.928	0.4757	0.8281	351.71	38.951	0.3962	0.3152
04 (VWF-12)	265.75	38.887	0.5686	1.0815	286.20	41.288	0.4870	0.3170
01 (HSA)	140.13	32.713	0.2556	0.7177	129.02	35.231	0.2819	0.3267
02 (HSA)	208.31	32.561	0.3147	0.6895	239.44	35.041	0.3067	0.3520
03 (HSA)	105.12	33.785	0.3360	0.8264	101.09	37.194	0.3603	0.3420
04 (HSA)	84.231	34.742	0.4123	0.9416	83.883	38.994	0.4348	0.3649

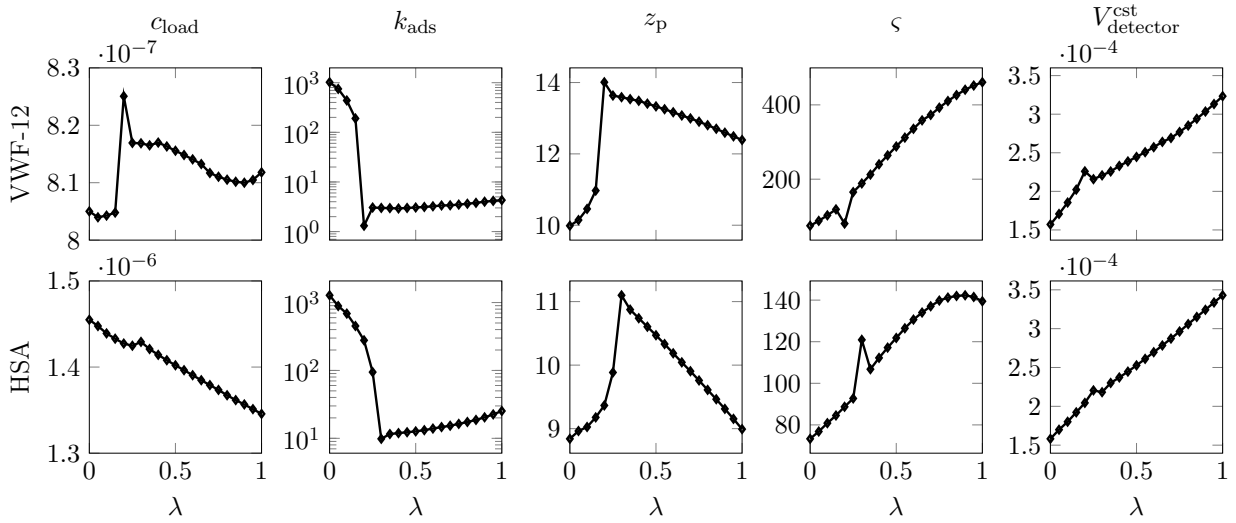

Figure 9: Parameter estimates along the homotopy path for VWF-12 (top) and HSA (bottom).

compared to simply choosing the previously determined estimate, as we do.

Interestingly, although the parameter $z_{\text{p,HSA}}$ varies between 9 and 11, at the end of the homotopy this parameter value is almost the same as in the beginning. This serves as an example that generally we cannot predict the behavior of the parameters along the homotopy. However, this was to be expected, due to, e.g., the highly nonlinear models being used.

Moreover, it is worth noting that the estimated detector volumes $V_{\text{detector}}^{\text{cst}}$ are quite similar. This is a promising result, as this parameter is independent of the actual component and it justifies our approach of estimating this parameter in combination with the other remaining parameters.

When taking a look at the required number of Gauss–Newton iterations, compare figure 10, we observe that for most parts convergence can be achieved within a couple of iterations, particularly in the last two thirds of the homotopy. However, in the first third of the homotopy more iterations are required and in one or two cases the maximum allowed number of iterations is reached. Nonetheless, as already discussed previously, we can still follow the homotopy until the end.

To conclude the description of the calibration procedure, we depict in figures 11 and 12 the real-

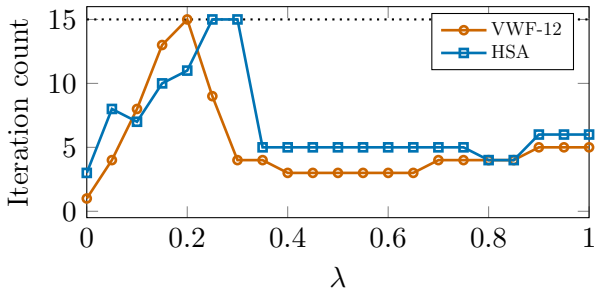

Figure 10: Required number of Gauss–Newton iterations for each instance along the homotopy.

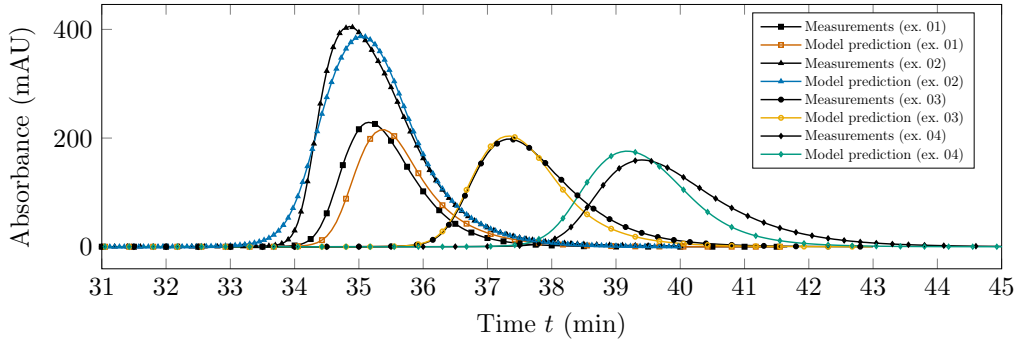

Figure 11: Real-world measurements (black) and corresponding model predictions (colored) for VWF-12 obtained by using the optimized parameters reported in table 3.

world measurements and the model predictions obtained when using the final parameter estimates, compare table 3.

We observe that the model predictions fit the real-world measurements exceptionally well in many cases, particularly for HSA. This is also remarkable insofar as the measurements for HSA show slight "bumps" in the rear part. For VWF-12 the model predictions are visibly more off, but still good results can be achieved. Interestingly, at least to the eye, the model prediction seems to agree best for experiment 03, both for VWF-12 and HSA. We furthermore remark that the parameters k_{ads} and z_{p} are almost completely correlated, both for VWF-12 and HSA, which was also observed by Rischawy et al. (2019) in their case study with different substances.

We conclude the section with an outlook on the usefulness of the obtained parameter estimates. We remark that since we have two estimates for the detector volume $V_{\text{detector}}^{\text{cst}}$, we use their arithmetic mean for the applied value.

To check the usefulness of the computed parameter estimates, we perform an experiment using a 1:1 (w/w) mixture of VWF-12 and HSA and where a salt gradient of 20 minutes duration is employed. Note that this experiment has not been used for calibration. We visualize the results in figure 13, where we depict both the UV absorbance and the conductivity signal. The model prediction for the latter is computed via an affine linear function with NaCl being the variable.

Comparing the measurement data with the respective single-component experiments, we note that HSA elutes earlier, namely during sample injection. This can be explained by the fact that the NaCl concentration of the sample buffer is higher than in the single-component case for HSA, namely 0.1484 M. At this higher salt concentration, HSA is not so strongly retained. Correspondingly, the

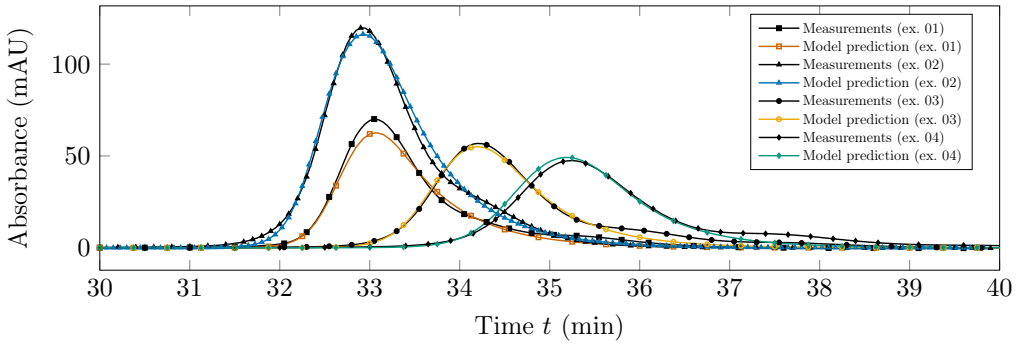

Figure 12: Real-world measurements (black) and corresponding model predictions (colored) for HSA obtained by using the optimized parameters reported in table 3.

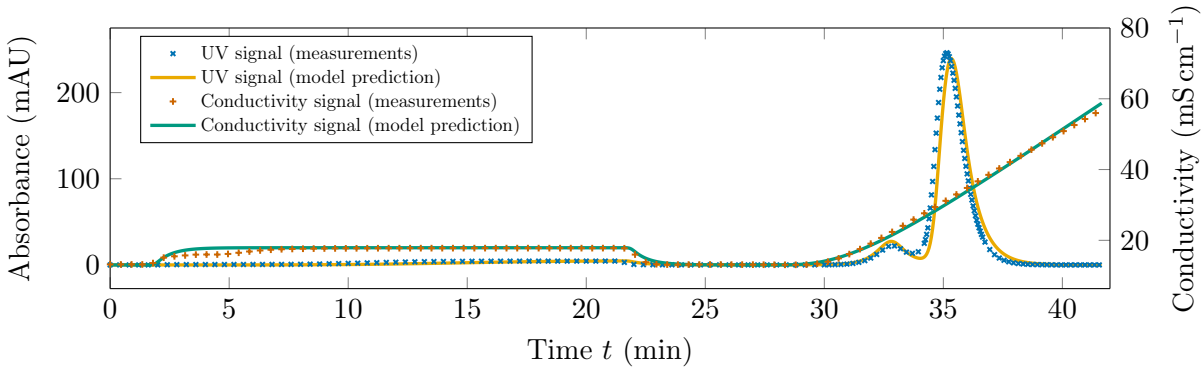

Figure 13: Measurement data and model predictions (UV absorbance and conductivity) obtained from a bind-and-elute experiment using a 1:1 (w/w) mixture of VWF-12 and HSA and a 20 minutes salt gradient. The employed model parameters are summarized in table 3.

peak signifying the eluting HSA at $t \approx 33\,\text{min}$ is smaller than the peak where HSA is investigated alone, compare figure 12.

We highlight that our UV model prediction shows an earlier eluting HSA component, too, although the substance starts eluting a little bit later in the prediction, compared to the real-world data. Furthermore, we observe that the smaller peak is also captured quite well. We therefore conclude that the estimated parameters indeed lead to promising results, at least for this experiment. However, we have to acknowledge that the applied salt gradient has also been used in single-component experiments. We should hence also check whether we obtain good predictions with the calibrated model when a salt gradient is used that is not covered by the experiments used for parameter estimation. Indeed, we have shown elsewhere that the real-world process presented in this case study can successfully be optimized, even when applying a salt gradient that is much steeper than the gradients used for calibration. For further details we refer to Cebulla et al. (2023).

4. Conclusion and outlook

In this work we developed a novel homotopy-based globalization approach for iterative solution methods for parameter estimation problems and specifically tailored to chromatographic applications. Afterwards, this approach has been used in combination with other methodologies to calibrate

a mathematical model describing a real-world IEX separation process where a product (VWF-12) is to be separated from an impurity (HSA).

The homotopy approach, which we primarily used to estimate adsorption-related parameters, works sufficiently well in practice. Indeed, we could obtain meaningful parameter estimates even though the respective initial parameter guesses were far away from the computed solution. Moreover, the generalized Gauss–Newton method typically converged in just few iterations for each instance along the homotopy. Even when convergence was not achieved within the prescribed iteration limit, it was still possible to reach the end of the homotopy. Furthermore, we note that only four different bind-and-elute experiments were required per substance to perform the parameter estimation procedure. This is indeed a small number of experiments.

Also, the prediction of the calibrated model lead to a good agreement with measurement data from a two-component experiment that was not used for parameter estimation. We again highlight that the calibrated model could also successfully be used for the optimization of the described IEX process (Cebulla et al., 2023).

We cannot overemphasize the fact that these promising results could be obtained even though the used column volume was just a fraction of the overall system volume.

Of course, further work can be considered regarding the presented homotopy approach. Most importantly, it must be examined how this method performs in practice when experimental data shows multiple peaks; such a generalized version has been shortly discussed in section 2.3.

Furthermore, in some cases it might be difficult to describe a peak with an EMG function, although generalizations have been proposed for more versatility (Purushothaman et al., 2017).

Lastly, in our case study we performed the homotopy with fixed step sizes which may lead to an exhaustive amount of (unnecessary) work. It definitively would be an improvement if the homotopy steps are chosen adaptively. The results shown in section 2.4 may serve as a starting point for a derivation of such an adaptive method.

Acknowledgments

The first, second, and fourth author gratefully acknowledge support by the German Federal Ministry for Education and Research under grants MOPhaPro (05M16VHA, 05M17MBA).

Conflicts of interest

The authors declare no conflicts of interest.

Abbreviations

CST continuous stirred tank

DPF dispersed plug flow

EMG exponentially modified Gaussian

IEX ion exchange chromatography

IPM interior point method

NLLS nonlinear least squares

NLP nonlinear program

ODE ordinary differential equation

PDE partial differential equation

SMA steric mass action

TDM transport-dispersive model

UV ultraviolet

Appendix

We summarize all model parameters obtained with the procedures described in section 3 in table 3. Furthermore, we depict in figures 14 and 15 selected concentration profiles when using the respective set of model parameters obtained along the homotopy path.

Table 3: Overview of estimated model parameters for the IEX separation process with VWF-12 and HSA, compare section 3. If applicable, 95% confidence intervals are stated, being computed via (11).

Parameter	Value	Unit	95% conf. interval	Obtained from ...
$L_{\text{system}}^{\text{dpf}}$	9.890×10^{1}	cm	$[9.874, 9.907] \times 10^{1}$	tracer experiments (section 3.2.1)
$r_{\text{system}}^{\text{dpf}}$	5.00×10^{-2}	cm	—	manufacturer
$D_{\text{ax, system}}^{\text{dpf}}$	3.212×10^{3}	$\text{cm}^2\,\text{min}^{-1}$	$[3.157, 3.267] \times 10^{3}$	tracer experiments (section 3.2.1)
$L_{\text{sample}}^{\text{dpf}}$	1.604×10^{2}	cm	—	tracer experiments (section 3.2.1)
$r_{\text{sample}}^{\text{dpf}}$	5.00×10^{-2}	cm	—	manufacturer
$D_{\text{ax, sample}}^{\text{dpf}}$	3.212×10^{3}	$\text{cm}^2\,\text{min}^{-1}$	—	tracer experiments (section 3.2.1)
$L_{\text{conn}}^{\text{dpf}}$	1.156×10^{2}	cm	$[1.155, 1.157] \times 10^{2}$	tracer experiments (section 3.2.1)
$r_{\text{conn}}^{\text{dpf}}$	3.75×10^{-2}	cm	—	manufacturer
$D_{\text{ax, conn}}^{\text{dpf}}$	2.72×10^{2}	$\text{cm}^2\,\text{min}^{-1}$	$[2.517, 2.921] \times 10^{2}$	tracer experiments (section 3.2.1)
$V_{\text{mixer}}^{\text{cst}}$	1.234×10^{0}	mL	$[1.561, 1.585] \times 10^{-1}$	tracer experiments (section 3.2.1)
$V_{\text{detector}}^{\text{cst}}$	3.277×10^{-1}	mL	—	bind-and-elute experiments (section 3.3); using arithmetic mean of estimates
L_c	2.50×10^{0}	cm	—	manufacturer
r_c	2.50×10^{-1}	cm	—	manufacturer
D_{ax}	2.753×10^{-2}	$\text{cm}^2\,\text{min}^{-1}$	—	Schmidt-Traub et al. (2012, eq. 6.165)
$c_{\text{load,VWF-12}}$	8.011×10^{-7}	M	$[7.925, 8.098] \times 10^{-7}$	bind-and-elute experiments (section 3.3)
$c_{\text{load,HSA}}$	1.352×10^{-6}	M	$[1.345, 1.359] \times 10^{-6}$	bind-and-elute experiments (section 3.3)
$\varepsilon_{\text{VWF-12}}^{(280)}$	1.0854×10^{5}	$\text{M}^{-1}\,\text{cm}^{-1}$	—	linear regression (section 3.2.2))
$\varepsilon_{\text{HSA}}^{(280)}$	1.5628×10^{4}	$\text{M}^{-1}\,\text{cm}^{-1}$	—	linear regression (section 3.2.2)
ℓ_{cp}	2.00×10^{-1}	cm	—	manufacturer
ε_b	3.70×10^{-1}	—	—	Schmidt-Traub et al. (2012, page 15)
ε_p	8.00×10^{-1}	—	—	moment analysis (12)
r_p	2.00×10^{-3}	cm	—	manufacturer
$k_{\text{eff,VWF-12}}$	3.56×10^{-2}	$\text{cm}\,\text{min}^{-1}$	—	correlations (13)
$k_{\text{eff,HSA}}$	2.93×10^{-2}	$\text{cm}\,\text{min}^{-1}$	—	correlations (13)
$k_{\text{eff,salt}}$	1.50×10^{-1}	$\text{cm}\,\text{min}^{-1}$	—	choice (section 3.2.2)
$k_{\text{ads,VWF-12}}$	6.412×10^{0}	$\text{M}^{-x}\,\text{min}^{-1}$ $(\star)$	$[4.867, 7.957] \times 10^{0}$	bind-and-elute experiments (section 3.3)
$k_{\text{ads,HSA}}$	1.330×10^{1}	$\text{M}^{-y}\,\text{min}^{-1}$ $(\star)$	$[1.198, 1.462] \times 10^{1}$	bind-and-elute experiments (section 3.3)
$k_{\text{des,VWF-12}}$	1.00×10^{8}	$\text{M}^{-x}\,\text{min}^{-1}$ $(\star)$	—	choice (section 3.3)
$k_{\text{des,HSA}}$	1.00×10^{8}	$\text{M}^{-y}\,\text{min}^{-1}$ $(\star)$	—	choice (section 3.3)

Continued on next page...

Table 3: Continued from previous page.

Parameter	Value	Unit	95% conf. interval	Obtained from ...
$z_{\mathrm{p,VWF\text{-}12}}$	1.218×10^{1}	—	$[1.203, 1.232] \times 10^{1}$	bind-and-elute experiments (section 3.3)
$z_{\mathrm{p,HSA}}$	9.290×10^{0}	—	$[9.242, 9.337] \times 10^{0}$	bind-and-elute experiments (section 3.3)
$\varsigma_{\mathrm{VWF\text{-}12}}$	4.663×10^{2}	—	$[4.461, 4.865] \times 10^{2}$	bind-and-elute experiments (section 3.3)
ς_{HSA}	1.379×10^{2}	—	$[1.331, 1.428] \times 10^{2}$	bind-and-elute experiments (section 3.3)
Λ_{IEX}	1.37×10^{0}	M	—	titration experiments (section 3.2.2)

$^{(\star)}$ $x = z_{\mathrm{p,VWF\text{-}12}}$, $y = z_{\mathrm{p,HSA}}$

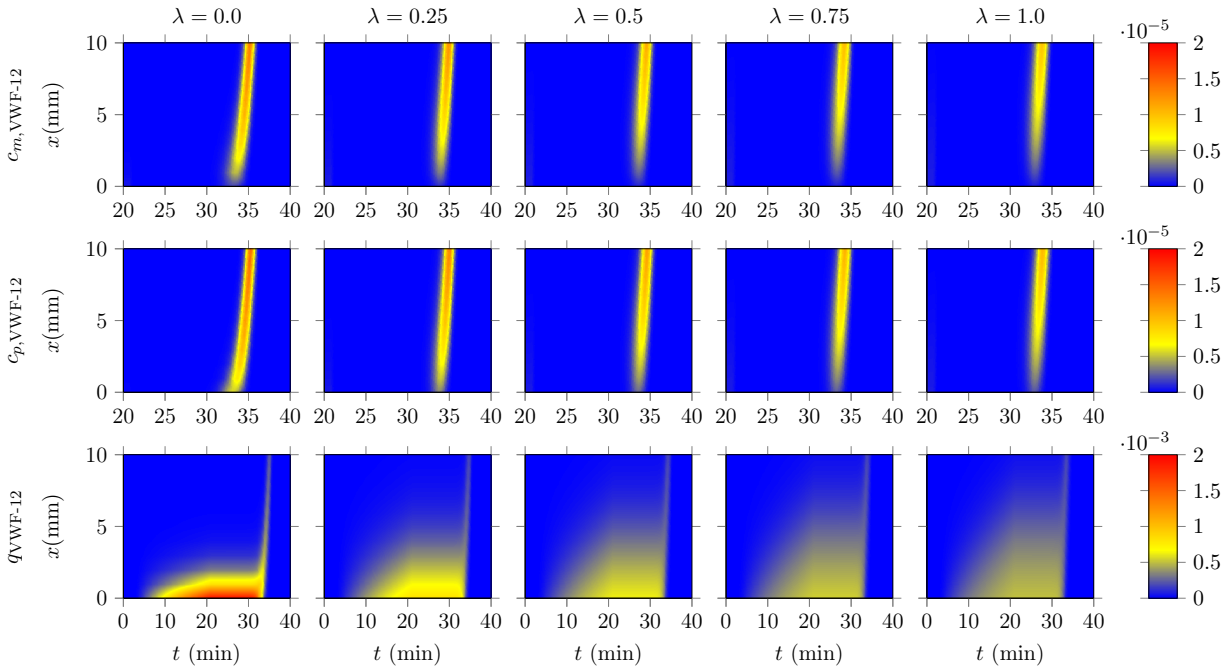

Figure 14: Selected concentration profiles for VWF-12 when using model parameters estimated along the homotopy path, here using a salt gradient of 20 min (that is, experiment 01, compare section 3.3). Note that different time axes are used for to make the changes more visible. For the same reason, the spatial dimension has been cropped to $x \in [0, 10]$ instead of $x \in [0, 25]$.

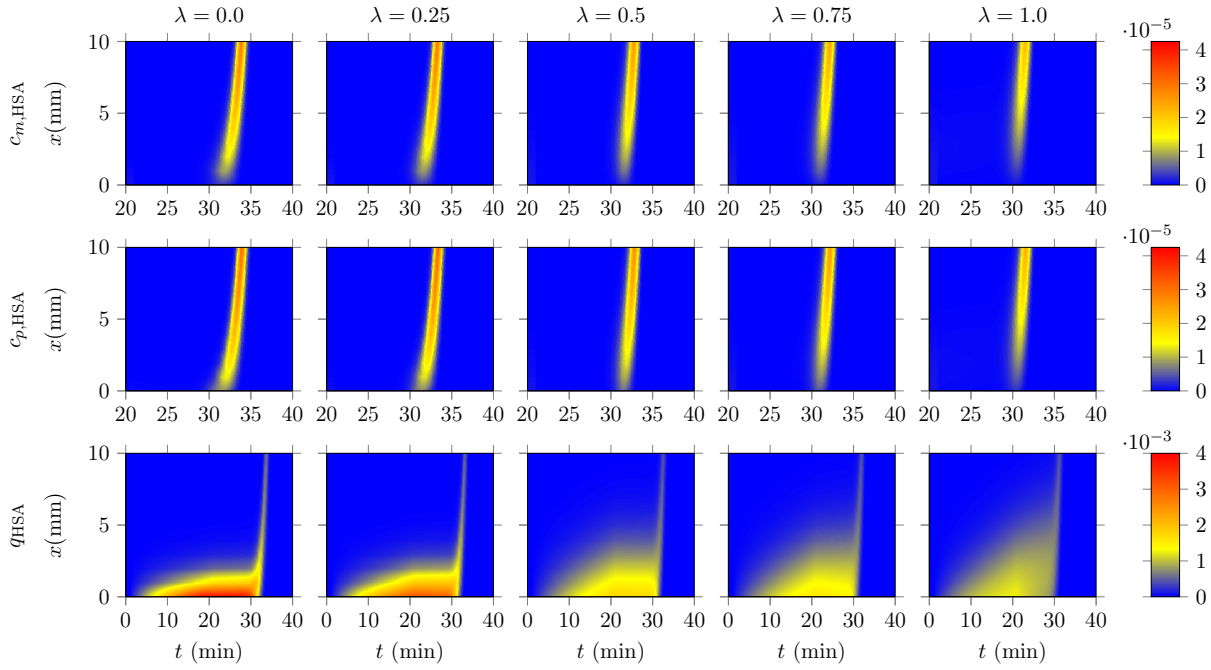

Figure 15: Selected concentration profiles for HSA when using model parameters estimated along the homotopy path, here using a salt gradient of 20 min (that is, experiment 01, compare section 3.3). Note that different time axes are used for to make the changes more visible. For the same reason, the spatial dimension has been cropped to $x \in [0, 10]$ instead of $x \in [0, 25]$.

References

Allgower, E.L., Georg, K., 1990. Numerical Continuation Methods. volume 13 of *Springer Series in Computational Mathematics*. Springer, Berlin, Heidelberg.

Bock, H.G., 1987. Randwertproblemmethoden zur Parameteridentifizierung in Systemen nichtlinearer Differentialgleichungen. volume 183 of *Bonner Mathematische Schriften*. Universität Bonn, Bonn.

Bock, H.G., Cebulla, D.H., Kirches, C., Potschka, A., 2021. Mixed-integer optimal control for multimodal chromatography. Comput. Chem. Eng. 153, 107435. URL: https://doi.org/10.1016/j.compchemeng.2021.107435, doi:10.1016/j.compchemeng.2021.107435.

Bock, H.G., Gutekunst, J., Potschka, A., Suaréz Garcés, M.E., 2020. A flow perspective on nonlinear least-squares problems. Vietnam J. Math. 48, 987–1003. URL: https://10.1007/s10013-020-00441-z, doi:10.1007/s10013-020-00441-z.

Bock, H.G., Kostina, E., Schlöder, J.P., 2007. Numerical methods for parameter estimation in nonlinear differential algebraic equations. Gamm-Mitt. 30, 376–408. URL: https://doi.org/10.1002/gamm.200790024, doi:10.1002/gamm.200790024.

Bock, H.G., Plitt, K.J., 1984. A multiple shooting algorithm for direct solution of optimal control problems. IFAC Proceedings Volumes 17, 1603–1608. URL: https://doi.org/10.1016/S1474-6670(17)61205-9, doi:10.1016/S1474-6670(17)61205-9. 9th IFAC World Congress: A Bridge Between Control Science and Technology, Budapest, Hungary, 2-6 July 1984.

Borg, N., Westerberg, K., Schnittert, S., von Lieres, E., Nilsson, B., 2012. Numerical analysis of model parameter uncertainties as a result of experimental uncertainty — An example from preparative chromatography, in: IFAC Proceedings Volumes, pp. 991–995. URL: https://doi.org/10.3182/20120215-3-AT-3016.00175, doi:10.3182/20120215-3-AT-3016.00175. 7th Vienna International Conference on Mathematical Modelling.

Brooks, C.A., Cramer, S.M., 1992. Steric mass-action ion exchange: Displacement profiles and induced salt gradients. AIChE J. 38, 1969–1978. URL: https://doi.org/10.1002/aic.690381212, doi:10.1002/aic.690381212.

Cebulla, D.H., Kirches, C., Kümmerer, N., Potschka, A., 2023. Model-based optimization of an ion exchange chromatography process for the separation of von Willebrand factor fragments and human serum albumin, in: Proceedings of the 93rd Annual Meeting of the International Association of Applied Mathematics and Mechanics, p. e202300027. URL: https://onlinelibrary.wiley.com/doi/abs/10.1002/pamm.202300027, doi:10.1002/pamm.202300027.

Cebulla, D.H., Kirches, C., Potschka, A., 2019. Parameter identifiability in a novel kinetic adsorption isotherm for multi-modal chromatography, in: Proceedings of the 58th IEEE Conference on Decision and Control (CDC), pp. 4755–4760. URL: https://doi.org/10.1109/CDC40024.2019.9029813, doi:10.1109/CDC40024.2019.9029813.

Danckwerts, P.V., 1953. Continuous flow systems: Distribution of residence times. Chem. Eng. Sci. 2, 1–13. URL: https://doi.org/10.1016/0009-2509(53)80001-1, doi:10.1016/0009-2509(53)80001-1.

Deitcher, R.W., Rome, J.E., Gildea, P.A., O'Connell, J.P., Fernandez, E.J., 2010. A new thermodynamic model describes the effects of ligand density and type, salt concentration and protein species in hydrophobic interaction chromatography. J. Chromatogr. A 1217, 199–208. URL: https://doi.org/10.1016/j.chroma.2009.07.068, doi:10.1016/j.chroma.2009.07.068.

Deuflhard, P., 2004. Newton Methods for Nonlinear Problems. volume 35 of *Springer Series in Computational Mathematics*. Springer, Berlin, Heidelberg. URL: https://doi.org/10.1007/978-3-642-23899-4, doi:10.1007/978-3-642-23899-4.

Foley, J.P., Dorsey, J.G., 1984. A review of the exponentially modified Gaussian (EMG) function: Evaluation and subsequent calculation of universal data. J. Chromatogr. Sci. 22, 40–46. URL: https://doi.org/10.1093/chromsci/22.1.40, doi:10.1093/chromsci/22.1.40.

Grushka, E., 1972. Characterization of exponentially modified Gaussian peaks in chromatography. Anal. Chem. 44, 1733–1738. URL: https://doi.org/110.1021/ac60319a011, doi:10.1021/ac60319a011.

Gu, T., 2015. Mathematical Modeling and Scale-Up of Liquid Chromatography. 2 ed., Springer, Cham. doi:10.1007/978-3-319-16145-7.

Guiochon, G., Felinger, A., Shirazi, D.G., Katti, A.M., 2006. Fundamentals of Preparative and Nonlinear Chromatography. 2 ed., Elsevier/Academic Press, Amsterdam.

Hahn, T., Baumann, P., Huuk, T., Heuveline, V., Hubbuch, J., 2016. UV absorption-based inverse modeling of protein chromatography. Eng. Life Sci. 16, 99–106. URL: https://doi.org/10.1002/elsc.201400247, doi:10.1002/elsc.201400247.

Hohmann, A., 1993. Inexact Gauss Newton Methods for Parameter Dependent Nonlinear Problems. Ph.D. thesis. Freie Universität Berlin. ZIB-Report TR-93-13, URN: urn:nbn:de:0297-zib-5049.

Holmqvist, A., Magnusson, F., Nilsson, B., 2015. Dynamic multi-objective optimization of batch chromatographic separation processes, in: Gernaey, K.V., Huusom, J.K., Gani, R. (Eds.), 12th International Symposium on Process Systems Engineering and 25th European Symposium on Computer Aided Process Engineering. Elsevier. volume 37 of *Computer Aided Chemical Engineering*, pp. 815–820. URL: https://doi.org/10.1016/B978-0-444-63578-5.50131-6, doi:10.1016/B978-0-444-63578-5.50131-6.

Kannicht, C., Solecka-Witulska, B., Winge, S., Schwientek, T., 2017. Glycosylated VWF fusion proteins with improved pharmacokinetics. URL: https://patentscope.wipo.int/search/en/detail.jsf?docId=WO2017198435. wO patent WO/2017/198435 (November 23, 2017).

Karlsson, D., Jakobsson, N., Axelsson, A., Nilsson, B., 2004. Model-based optimization of a preparative ion-exchange step for antibody purification. J. Chromatogr. A 1055, 29–39. URL: https://doi.org/10.1016/j.chroma.2004.08.151, doi:10.1016/j.chroma.2004.08.151.

Leweke, S., von Lieres, E., 2018. Chromatography analysis and design toolkit (CADET). Comput. Chem. Eng. 113, 274–294. URL: https://doi.org/10.1016/j.compchemeng.2018.02.025, doi:10.1016/j.compchemeng.2018.02.025.

Nfor, B.K., Noverraz, M., Chilamkurthi, S., Verhaert, P.D.E.M., van der Wielen, L.A.M., Ottens, M., 2010. High-throughput isotherm determination and thermodynamic modeling of protein adsorption on mixed mode adsorbents. J. Chromatogr. A 1217, 6829–6850. URL: https://doi.org/10.1016/j.chroma.2010.07.069, doi:10.1016/j.chroma.2010.07.069.

Nfor, B.K., Zuluaga, D.S., Verheijen, P.J.T., Verhaert, P.D.E.M., van der Wielen, L.A.M., Ottens, M., 2011. Model-based rational strategy for chromatographic resin selection. Biotechnol. Progr. 27, 1629–1643. URL: https://doi.org/10.1002/btpr.691, doi:10.1002/btpr.691.

Nilsson, B., Andersson, N., 2017. Simulation of process chromatography, in: Staby, A., Rathore, A.S., Ahuja, S. (Eds.), Preparative Chromatography for Separation of Proteins. John Wiley & Sons. chapter 3, pp. 81–110. URL: https://doi.org/10.1002/9781119031116.ch3, doi:10.1002/9781119031116.ch3.

Nocedal, J., Wright, S.J., 2006. Numerical Optimization. 2 ed., Springer, Berlin, Heidelberg, New York.

Osberghaus, A., Hepbildikler, S., Nath, S., Haindl, M., von Lieres, E., Hubbuch, J., 2012a. Determination of parameters for the steric mass action model—A comparison between two approaches. J. Chromatogr. A 1233, 54–65. URL: https://doi.org/10.1016/j.chroma.2012.02.004, doi:10.1016/j.chroma.2012.02.004.

Osberghaus, A., Hepbildikler, S., Nath, S., Haindl, M., von Lieres, E., Hubbuch, J., 2012b. Optimizing a chromatographic three component separation: A comparison of mechanistic and empiric modeling approaches. J. Chromatogr. A 1237, 86–95. URL: https://doi.org/10.1016/j.chroma.2012.03.029, doi:10.1016/j.chroma.2012.03.029.

Persson, P., Gustavsson, P.E., Zacchi, G., Nilsson, B., 2006. Aspects of estimating parameter dependencies in a detailed chromatography model based on frontal experiments. Process Biochem. 41, 1812–1821. URL: https://doi.org/10.1016/j.procbio.2006.03.030, doi:10.1016/j.procbio.2006.03.030.

Pirrung, S.M., van der Wielen, L.A.M., van Beckhoven, R.F.W.C., van de Sandt, E.J.A.X., Eppink, M.H.M., Ottens, M., 2017. Optimization of biopharmaceutical downstream processes supported by mechanistic models and artificial neural networks. Biotechnol. Progr. 33, 696–707. URL: https://doi.org/10.1002/btpr.2435, doi:10.1002/btpr.2435.

Polson, A., 1950. Some aspects of diffusion in solution and a definition of a colloidal particle. J. Phys. Colloid Chem. 54, 649–652. URL: https://doi.org/10.1021/j150479a007, doi:10.1021/j150479a007.

Potschka, A., Bock, H.G., 2021. A sequential homotopy method for mathematical programming problems. Math. Progam. Ser. A 187, 459–486. URL: https://doi.org/10.1007/s10107-020-01488-z, doi:10.1007/s10107-020-01488-z.

Purushothaman, S., Ayet San Andrés, S., Bergmann, J., Dickel, T., Ebert, J., Geissel, H., Hornung, C., Plaß, W.R., Rappold, C., Scheidenberger, C., Tanaka, Y.K., Yavor, M.I., 2017. Hyper-EMG: A new probability distribution function composed of Exponentially Modified Gaussian distributions to analyze asymmetric peak shapes in high-resolution time-of-flight mass spectrometry. Int. J. Mass Spectrom. 421, 245–254. URL: https://doi.org/10.1016/j.ijms.2017.07.014, doi:10.1016/j.ijms.2017.07.014.

Rathore, A.S., Kumar, D., Kateja, N., 2018. Recent developments in chromatographic purification of biopharmaceuticals. Biotechnol. Lett. 40, 895–905. URL: https://doi.org/10.1007/s10529-018-2552-1, doi:10.1007/s10529-018-2552-1.

Rischawy, F., Saleh, D., Hahn, T., Oelmeier, S., Spitz, J., Kluters, S., 2019. Good modeling practice for industrial chromatography: Mechanistic modeling of ion exchange chromatography of a bispecific antibody. Comput. Chem. Eng. 130, 106532. URL: https://doi.org/10.1016/j.compchemeng.2019.106532, doi:10.1016/j.compchemeng.2019.106532.

Sandoval, G., Andrews, B.A., Asenjo, J.A., 2012. Elution relationships to model affinity chromatography using a general rate model. J. Mol. Recognit. 25, 571–579. URL: https://doi.org/10.1002/jmr.2223, doi:10.1002/jmr.2223.

Schlöder, J.P., 1988. Numerische Methoden zur Behandlung hochdimensionaler Aufgaben der Parameteridentifizierung. volume 187 of *Bonner Mathematische Schriften*. Universität Bonn, Bonn.

Schmidt-Traub, H., Schulte, M., Seidel-Morgenstern, A. (Eds.), 2012. Preparative Chromatography. 2 ed., Wiley–VCH, Weinheim.

Smith, R.C., 2013. Uncertainty Quantification: Theory, Implementation, and Applications. volume 12 of *Computational Science and Engineering Series*. Society for Industrial and Applied Mathematics, Philadelphia, PA.

Tugcu, N., Bae, S.S., Moore, J.A., Cramer, S.M., 2002. Stationary phase effects on the dynamic affinity of low-molecular-mass displacers. J. Chromatogr. A 954, 127–135. URL: https://doi.org/10.1016/S0021-9673(02)00164-4, doi:10.1016/S0021-9673(02)00164-4.

Unger, K.K., Ditz, R., Machtejevas, E., Skudas, R., 2010. Liquid chromatography — Its development and key role in life science applications. Angew. Chem. Int. Ed. 49, 2300–2312. URL: https://doi.org/110.1002/anie.200906976, doi:10.1002/anie.200906976.

U.S. Food and Drug Administration, 2004. Guidance for industry: PAT—A framework for innovative pharmaceutical development, manufacturing, and quality assurance. URL: https://www.fda.gov/media/71012/download.

Vollack-Hesse, N., Oleshko, O., Werwitzke, S., Solecka-Witulska, B., Kannicht, C., Tiede, A., 2021. Recombinant VWF fragments improve bioavailability of subcutaneous factor VIII in hemophilia A mice. Blood 137, 1072–1081. URL: https://doi.org/10.1182/blood.2020006468, doi:10.1182/blood.2020006468.

Wang, G., Hahn, T., Hubbuch, J., 2016. Water on hydrophobic surfaces: Mechanistic modeling of hydrophobic interaction chromatography. J. Chromatogr. A 1465, 71–78. URL: https://doi.org/10.1016/j.chroma.2016.07.085, doi:10.1016/j.chroma.2016.07.085.